Inorganic Chemistry

Article

pubs.acs.org/IC

Pushing the Limits of Delta Bonding in Metal−Chromium Complexes with Redox Changes and Metal Swapping

Reed J. Eisenhart,[†,‡] P. Alex Rudd,[†,‡] Nora Planas,[†,§] David W. Boyce,[†] Rebecca K. Carlson,[†,§] William B. Tolman,[†] Eckhard Bill,*[,∥] Laura Gagliardi,*[,†,§] and Connie C. Lu*[,†]

[†]Department of Chemistry and [§]Supercomputing Institute and Chemical Theory Center, University of Minnesota, Minneapolis, Minnesota 55455, United States

[∥]Max Planck Institut für Chemische Energiekonversion (MPI-CEC), Stiftstraße 34−36, 45470 Mülheim an der Ruhr, Germany

Supporting Information

ABSTRACT: Into the metalloligand Cr[N(*o*-(NCH$_2$P(^{i}Pr)$_2$)-C$_6$H$_4$)$_3$] (**1**, CrL) was inserted a second chromium atom to generate the dichromium complex Cr$_2$L (**2**), which is a homobimetallic analogue of the known MCrL complexes, where M is manganese (**3**) or iron (**4**). The cationic and anionic counterparts, [MCrL]$^+$ and [MCrL]$^-$, respectively, were targeted, and each MCr pair was isolated in at least one other redox state. The solid-state structures of the [MCrL]$^{+,0,-}$ redox members are essentially the same, with ultrashort metal−metal bonds between 1.96 and 1.74 Å. The formal shortness ratios (*r*) of these interactions are between 0.84 and 0.74 and are interpreted as triple to quintuple metal−metal bonds with the aid of theory. The trio of (d−d)^{10} species [Cr$_2$L]$^-$ (**2**^{red}), MnCrL (**3**), and [FeCrL]$^+$ (**4**^{ox}) are S = 0 diamagnets. On the basis of M—Cr bond distances and theoretical calculations, the strength of the metal−metal bond across the (d−d)^{10} series increases in the order Fe < Mn < Cr. The methylene protons in the ligand are shifted downfield in the ^{1}H NMR spectra, and the diamagnetic anisotropy of the metal−metal bond was calculated as -3500×10^{-36}, -3900×10^{-36}, and -5800×10^{-36} m^3 molecule^{-1} for **2**^{red}, **3**, and **4**^{ox} respectively. The magnitude of diamagnetic anisotropy is, thus, affected more by bond polarity than by bond order. A comparative vis−NIR study of quintuply bonded **2**^{red} and **3** revealed a large red shift in the $\delta^4 \rightarrow \delta^3\delta^*$ transition energy upon swapping from the (Cr$_2$)$^{2+}$ to the (MnCr)$^{3+}$ core. Complex **2**^{red} was further investigated by resonance Raman spectroscopy, and a band at 434 cm^{-1} was assigned as the Cr—Cr bond vibration. Finally, **4**^{ox} exhibited a Mössbauer doublet with an isomer shift of 0.18 mm/s that suggests a primarily Fe-based oxidation to Fe(I).

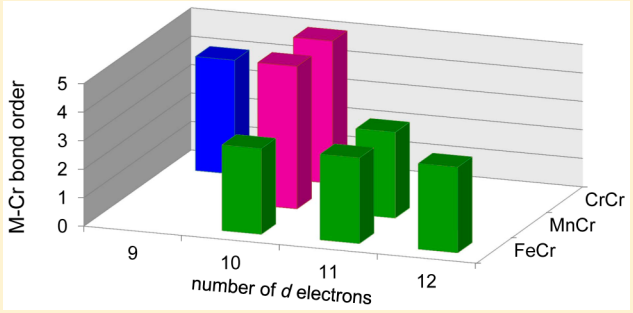

INTRODUCTION

The chemical bond is arguably the most fundamental yet evolving concept in chemistry.[1] Although the notation of the delta bond was developed in 1929,[2] the first structural evidence of the delta bond came in 1964 when a quadruple bond ($\sigma + 2\pi + \delta$) was invoked to explain the short Re−Re distance and eclipsed conformation in [Re$_2$Cl$_8$]$^{2-}$.[3] Since this seminal discovery, studies of metal−metal multiple bonds have flourished and traversed a number of disciplines. Physical chemists coupled new methodologies to generate and interrogate bare, or unligated, dinuclear metal clusters, to understand the bonding, electronic structures, and spectroscopic properties of metal−metal bonds across the periodic table.[4] These efforts were heavily aided by theorists, who improved the accuracy of their predictions by developing new electronic structure theories to address the problems of electron correlation.[5]

In a momentous discovery, a complex with a quintuply bonded ($\sigma + 2\pi + 2\delta$) dichromium unit was isolated using bulky terphenyl ligands.[6] Today, the coordination chemistry of the quintuple bond comprises several dichromium, a few dimolybdenum, and a single MnCr heterobimetallic species.[7] The reactivities of these quintuply bonded species are currently being explored, and initial studies show promise as inorganic counterparts to the wider reactivity of unsaturated carbon−carbon bonds.[7,8]

Heterometallic multiple bonds involving exclusively first-row transition metals have been reported by Thomas and coworkers[9] and by some of us.[10] Starting from the monochromium complex Cr(N(*o*-(NCH$_2$P^{i}Pr$_2$)C$_6$H$_4$)$_3$) (abbreviated as CrL, **1**), which acts as a metalloligand to bind a second transition metal, a series of MCr binuclear compounds was isolated for M = Mn, Fe, Co, and Ni. The series culminated in a quintuply bonded MnCr heterometallic species that opened the possibility of investigating metal substitution effects on delta bonding. In addition, the rich electrochemistry of the neutral MCr bimetallics gave us hope that redox counterparts with high bond multiplicity could be isolated and probed to understand the redox properties associated with delta bonding. To this end,

Received: May 27, 2015
Published: July 13, 2015

ACS Publications © 2015 American Chemical Society

DOI: 10.1021/acs.inorgchem.5b01163
Inorg. Chem. 2015, 54, 7579−7592

we report four additional members of the MCr series, including the homobimetallic dichromium complex Cr_2L (**2**) and the MCr cationic and/or anionic counterparts $[MCrL]^{+,-}$ for M = Cr, Mn, and Fe (Figure 1). In particular, the trio of $(d-d)^{10}$

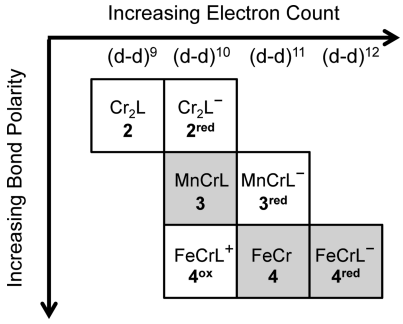

Figure 1. Metal−chromium complexes and their $(d-d)^n$ counts, where the polarity of the M—Cr bonds increases in the order Cr < Mn < Fe. White boxes represent new compounds. Previously reported complexes are shown in light gray boxes.

species comprising $[Cr_2L]^-$ ($\mathbf{2}^{red}$), MnCrL (**3**), and $[FeCrL]^+$ ($\mathbf{4}^{ox}$) form a unique group of isostructural and potentially isoelectronic bimetallics with multiple metal−metal bonds. These bimetallics of the mid-first-row transition metals were investigated through spectroscopic studies [nuclear magnetic resonance (NMR), electron paramagnetic resonance (EPR), resonance Raman (rR), and Mössbauer], complemented by quantum chemical calculations.

EXPERIMENTAL SECTION

General Considerations. Unless otherwise stated, all manipulations were performed inside a glovebox under a N_2 atmosphere or using standard Schlenk techniques. Standard solvents were deoxygenated by sparging with N_2 and dried by passing through activated alumina columns of an SG Water solvent purification system. Deuterated solvents were purchased from Cambridge Isotope Laboratories, degassed by freeze−pump−thaw cycles, and stored over activated 4 Å molecular sieves. The ligand $N(o\text{-}(NHCH_2P^iPr_2)\text{-}C_6H_4)_3$ (abbreviated as H_3L),[11] CrL (**1**),[10b] MnCrL (**3**),[10a] FeCrL (**4**),[10b] $Tl[B(3,5\text{-}(CF_3)_2C_6H_3)_4]$,[12] and $[FeCp_2][B(3,5\text{-}(CF_3)_2C_6H_3)_4]$ (where $FeCp_2$ represents ferrocene)[13,14] were synthesized according to literature procedures. Elemental analyses were performed by Complete Analysis Laboratories (Parsippany, NJ).

Synthesis of **2**, *$Cr_2(N(o\text{-}(NCH_2P^iPr_2)C_6H_4)_3)$*. A solution of **1** (0.115 g, 0.157 mmol) in tetrahydrofuran (THF; ca. 4 mL) was mixed with a stirred slurry of $CrCl_3$ (0.026 g, 0.16 mmol) in THF (ca. 4 mL) for 15 min, forming a homogeneous green solution. The solution was then added to KC_8 (0.064 g, 0.47 mmol). Within minutes, the solution turned dark brown, and a precipitate formed. After removal of the solvent in vacuo, the sample was dissolved in toluene and filtered through a Celite plug. The brown solution was dried in vacuo, yielding a brown powder (0.093 g, 76%), which was used without further purification. Single crystals of **2** were grown by diffusion of *n*-pentane into a concentrated solution of **2** in THF. ^{1}H NMR (ppm, C_6D_6, 500 MHz): 34.2, 10.9, 9.1, 5.0, 4.1, 3.4, 1.4, 1.2, 1.0, −0.5, −2.4, −15.2. UV−vis−NIR (THF) λ_{max} (nm) (ε (M^{-1} cm^{-1})): 495 (sh, 2330), 600 (1480), 880 (930), 1460 (140). Anal. Calcd for **2**, $C_{39}H_{60}N_4P_3Cr_2$: 59.91 C, 7.74 H, 7.17 N. Found: 59.79 C, 7.69 H, 7.09 N.

Synthesis of *$K[\mathbf{2}^{red}]$*, *$K[Cr_2(N(o\text{-}(NCH_2P^iPr_2)C_6H_4)_3)]$*. A solution of **1** (0.11 g, 0.15 mmol) in THF (ca. 4 mL) was mixed with a stirred slurry of $CrCl_3$ (0.024 g, 0.15 mmol) in THF (ca. 4 mL) for 15 min, forming a homogeneous green solution. The solution was then added to KC_8 (0.084 g, 0.62 mmol), forming a dark green solution with a precipitate. The sample was filtered through a Celite plug and dried in vacuo, yielding a crude green powder (0.12 g, 98%). Single crystals of $\mathbf{2}^{red}$ were grown by diffusion of *n*-pentane into a concentrated THF solution of $\mathbf{2}^{red}$. The ^{1}H NMR spectrum had extremely broad peaks at room temperature, indicative of fluxional behavior. ^{1}H NMR (ppm, THF-d_8, 500 MHz, −80 °C): 6.39 (t, *J* = 7 Hz, 1H), 6.15 (d, *J* = 7 Hz, 1H), 6.06(d, *J* = 7 Hz, 1H), 5.45 (t, *J* = 7 Hz, 1H), 5.28 (d, *J* = 12 Hz, 1H), 4.47 (d, *J* = 12 Hz, 1H), 2.73 (br, 1H), 2.63 (br, 1H), 1.85 (br, 3H), 1.54 (br, 3H), 1.21 (br, 3H), 0.27 (br, 3H). ^{13}C NMR (ppm, THF-d_8, 126 MHz, −80 °C): 157.6, 136.5, 126.5, 124.9, 106.4, 106.1, 67 (overlapping with solvent), 34.1, 29.1, 23.5, 21.2, 21.0, 19.0. ^{31}P NMR (ppm, THF-d_8, 200 MHz, −80 °C): 42.4. UV−vis−NIR (THF) λ_{max} (nm) (ε (M^{-1} cm^{-1})): 315 (18300), 675 (1880). Anal. Calcd for $K(\mathbf{2}^{red})$, $C_{39}H_{60}N_4P_3Cr_2K$: 57.06 C, 7.37 H, 6.82 N. Found: 56.97 C, 7.28 H, 6.69 N.

Synthesis of *$K(crypt\text{-}222)[\mathbf{3}^{red}]$*, *$[K(crypt\text{-}222)][MnCr(N(o\text{-}(NHCH_2P^iPr_2)C_6H_4)_3)]$*. A solution of **1** (0.12 g, 0.16 mmol) in THF (ca. 4 mL) was mixed with a stirred slurry of $MnBr_2$ (0.027 g, 0.17 mmol) in THF (ca. 4 mL) for 15 min, forming a homogeneous green solution. Solid KC_8 (0.057 g, 0.51 mmol) was then added. Within minutes, the solution turned dark red-brown, and a precipitate formed. After removal of the solvent in vacuo, the sample was washed with toluene (ca. 1 mL), reconstituted in THF (ca. 2 mL), and filtered through a Celite plug into a solution of 2.2.2-cryptand (crypt-222; 0.049 g, 0.16 mmol) in THF (ca. 2 mL). The solution was dried in vacuo and washed with Et_2O (ca. 4 mL). An alternative synthesis procedure was also employed as follows: To a solution of **3** (0.038 g, 0.048 mmol) in THF (ca. 4 mL) was added solid KC_8 (0.0065 g, 0.048 mmol). Within minutes, the initial red-brown color of the solution turned yellow-brown. After the solution had been filtered through a glass filter, the filtrate was mixed with crypt-222 (0.018 g, 0.0477 mmol) and stirred for 10 min; the solvent was then removed in vacuo to yield 54 mg of $\mathbf{3}^{red}$ (0.045 mmol, 94% crude yield). Single crystals of $\mathbf{3}^{red}$ (18 mg, 11% crystalline yield) were grown by diffusion of *n*-pentane into a concentrated THF solution of $\mathbf{3}^{red}$. ^{1}H NMR (ppm, THF-d_8, 500 MHz): 19.3, 17.2, 8.7, 7.8, 4.4, 3.5, 2.5, 1.1, 0.5, −6.6. UV−vis−NIR (THF) λ_{max} (nm) (ε (M^{-1} cm^{-1})): 745 (1230), 1350 (760). Anal. Calcd for $K(crypt\text{-}222)[\mathbf{3}^{red}]$, $[K(C_{18}H_{36}N_2O_6)][C_{39}H_{60}N_4P_3CrMn]$: 57.03 C, 8.06 H, 7.00 N. Found: 57.06 C, 8.14 H, 6.97 N.

Synthesis of *$\mathbf{4}^{ox}[B(Ar_F)_4]$*, *$[FeCr(N(o\text{-}(NCH_2P^iPr_2)C_6H_4)_3)][B(3,5\text{-}(CF_3)_2C_6H_3)_4]$*. A THF slurry (ca. 6 mL) of KC_8 (22.2 mg, 0.164 mmol) was added to a stirring solution of **1** (120 mg, 0.164 mmol) in 12 mL of THF at −78 °C. The mixture was warmed to room temperature, stirred for 5 min, and filtered. Solid $FeBr_2$ (20.8 mg, 0.164 mmol) was added to the stirring filtrate at −78 °C. The reaction mixture was warmed to room temperature and stirred until all of the $FeBr_2$ solid had reacted, ∼20 min. The reaction mixture was filtered, and the solvent was removed in vacuo. The crude residue was taken up in 4 mL of toluene, diluted with 10 mL of pentane, cooled to −20 °C, and filtered to remove a brown solid. This was repeated two more times, and then the solution was cooled to −20 °C overnight, from which a green crystalline powder, presumably $(Br)FeCr(N(o\text{-}(NCH_2P^iPr_2)C_6H_4)_3)$ (33.2 mg, 23% yield), was isolated. These crystals were dissolved in 4 mL of THF, and to this stirring solution was added dropwise $Tl[B(Ar_F)_4]$ (40.9 mg, 0.038 mmol) in 4 mL of Et_2O. After this mixture had been stirred for 20 min at room temperature, a gray solid was filtered off, and the filtrate was dried in vacuo, yielding 55 mg (0.033 mmol, 87% yield) of $\mathbf{4}^{ox}[B(Ar_F)_4]$. Single crystals of $\mathbf{4}^{ox}$ were grown by diffusion of *n*-pentane into a concentrated THF solution of $\mathbf{4}^{ox}$. ^{1}H NMR (ppm, THF-d_8, 500 MHz, 7 °C): 7.80 (s, 8H), 7.58 (s, 4H), 7.16 (t, *J* = 8 Hz, 3H), 7.11 (d, *J* = 8 Hz, 3H), 6.63 (d, *J* = 8 Hz, 3H), 6.48 (t, *J* = 8 Hz, 3H), 6.36 (s, 6H), 3.15 (br, 3H), 2.88 (br, 3H), 1.52 (m, 9H), 1.44 (m, 9H), 1.34 (m, 9H), 0.72 (m, 9H). ^{13}C NMR (ppm, THF-d_8, 126 MHz, −20 °C): 135.4 [aryl, $B(Ar_F)_4$], 128.6 (aryl), 126.6 (aryl), 120.9 (aryl), 118.1 [aryl, $B(Ar_F)_4$], 111 (aryl), 75.6 (CH_2), 32.8 (*CH*), 28.0 (*CH*), 22.4 (CH_3), 20.3 (CH_3), 19.4 (CH_3), 18.0 (CH_3) (note that quarternary carbons were not observed). ^{31}P NMR (ppm, THF-d_8, 126 MHz, 17 °C): 26.6. UV−vis−NIR (THF) λ_{max} (nm) (ε (M^{-1} cm^{-1})): 463 (4860), 730 (3890), 1495 (490). Anal. Calcd for $\mathbf{4}^{ox}[B(Ar_F)_4]$,

DOI: 10.1021/acs.inorgchem.5b01163
Inorg. Chem. 2015, 54, 7579−7592

Table 1. Crystallographic Details for Complexes of 1, 2, K[2^{red}], K(crypt-222)[3^{red}], and $4^{ox}[B(Ar_F)_4]$

	1	2	K[2^{red}]·THF	K(crypt-222)[3^{red}]	$4^{ox}[B(Ar_F)_4]$
chemical formula	$C_{39}H_{60}CrN_4P_3$	$C_{39}H_{60}N_4P_3Cr_2$	$C_{39}H_{60}N_4Cr_2P_3K{\cdot}C_4H_8O$	$C_{39}H_{60}N_4P_3MnCr{\cdot}C_{18}H_{36}N_2O_6K$	$C_{39}H_{60}N_4P_3FeCr{\cdot}C_{32}H_{12}F_{24}B$
formula weight	729.82	781.82	893.02	1200.35	1648.90
crystal system	monoclinic	trigonal	monoclinic	trigonal	triclinic
space group	$P2_1/n$	$P321$	Cc	$P\bar{3}$	$P\bar{1}$
a (Å)	11.1248(7)	16.067(3)	12.9903(19)	11.3119(7)	10.5449(8)
b (Å)	20.166(1)	16.067(3)	27.035(4)	11.3119(7)	18.5182(14)
c (Å)	17.373(1)	11.673(2)	14.055(2)	28.5164(18)	20.4402(16)
α (deg)	90	90	90	90	71.0960(10)
β (deg)	92.293(1)	90	93.906(2)	90	78.6720(10)
γ (deg)	90	120	90	120	87.5320(10)
V (Å^3)	3894.4(4)	2609.7(9)	4924.6(12)	3160.1(4)	3701.7(5)
Z	4	2	4	2	2
D_{calcd} (g cm^{-3})	1.245	0.995	1.204	1.262	1.479
λ (Å), μ (mm^{-1})	0.71073, 0.449	0.71073, 0.805	0.71073, 0.853	0.71073, 0.564	0.71073, 0.512
T (K)	173(2)	173(2)	173(2)	173(2)	123(2)
θ range (deg)	2.20−27.42	2.260−24.640	2.1945−24.658	2.184−27.486	2.207−27.2555
reflns collected	33608	6896	25827	33862	43571
unique reflns	6647	2958	9412	4397	10885
data/restraint/parameters	8993/0/436	6896/0/145	11248/0/487	4850/0/226	16967/762/1030
R1, wR2 [$I > 2\sigma(I)$]	0.0418, 0.0993	0.0466, 0.0903	0.0422, 0.0873	0.0296, 0.0689	0.1116, 0.3043

$[C_{39}H_{60}N_4P_3FeCr][C_{32}H_{12}F_{24}B]$: 51.72 C, 4.40 H, 3.40 N. Found: 51.67 C, 4.40 H, 3.26 N.

Physical Methods. ^{1}H NMR spectra were recorded on a Bruker 500 MHz spectrometer at room temperature unless otherwise stated. All ^{1}H and ^{13}C NMR spectra are referenced to the internal solvent residual. Variable-temperature NMR experiments were performed on a Bruker 500 MHz spectrometer. The temperature of the NMR probe was calibrated against an external methanol standard. Diamagnetic anisotropy ($\chi_{\parallel} - \chi_{\perp}$) was calculated as[15]

$$\Delta\delta = \left(\frac{1}{3r^3}\right)\frac{(\chi_{\parallel} - \chi_{\perp})[1 - 3\cos^2(\theta)]}{4\pi} \quad (1)$$

where $\Delta\delta$ is the difference in chemical shift (ppm) between the resonance in a bimetallic complex versus a reference complex, namely, the isostructural Ni−Al complex featuring a Ni → Al dative bond. The distance of the proton to the center of the metal−metal bond is r, and the acute angle between the proton and the metal−metal axis is θ [Table S2, Supporting Information (SI)]. The units are 10^{-36} m^3 molecule^{-1}. The barrier to inversion, $\Delta G^{\ddagger}$, was calculated as

$$\Delta G^{\ddagger} = RT_c\left[23.760 + \ln\left(\frac{T_c}{k_c}\right)\right] \quad (2)$$

where the coalescence temperature T_c is in kelvin; R is the ideal gas constant; and $k_c = [\pi(\Delta\nu_0)]/\sqrt{2}$, where $\Delta\nu_0$ is the difference in frequency (Hz) between the exchanging protons (Table S1, SI).[16] UV−vis−NIR spectra were collected at room temperature on a Cary-14 spectrometer. Cyclic voltammetry was conducted using a CH Instruments 600 electrochemical analyzer. The one-cell setup utilized a glassy carbon working electrode, Pt wire counter electrode, and Ag/$AgNO_3$ reference electrode in CH_3CN. Analyte solutions were prepared in a THF solution of 0.4 M [^{n}Bu$_4$N][PF_6] and referenced internally to the $FeCp_2^{0/+}$ redox couple. IR spectra were collected using a Bruker Tensor-37 FTIR instrument with OPUS 6.5 software. Perpendicular-mode X-band EPR spectra were recorded at 20 K with a Bruker ESP 300 spectrometer equipped with an Oxford ESR 910 liquid-helium cryostat and an Oxford temperature controller. X-band EPR spectra were simulated using the EPR program (version W95) written by Frank Neese (MPI-CEC, Mülheim, Germany). Mössbauer data were recorded on an alternating-constant acceleration spectrometer. The minimum experimental line width was 0.24 mm s^{-1} (full width at half-height). The sample temperature was maintained constant in an Oxford Instruments Variox or an Oxford Instruments Mössbauer-Spectromag 2000 cryostat, which is a split-pair superconducting magnet system for applied fields (up to 8 T). The field at the sample was oriented perpendicular to the γ-beam. The ^{57}Co/Rh source (1.8 GBq) was positioned at room temperature inside the gap of the magnet system at a zero-field position. Isomer shifts are quoted relative to iron metal at 300 K. Resonance Raman samples were prepared in a nitrogen-filled glovebox in dry THF and were immediately frozen in quartz tubes at −196 °C. Resonance Raman spectra were recorded on an Acton 506M3 spectrometer using a Princeton Instruments ACTON PyLoN LN/CCD-1340 × 400 detector. The spectra were obtained at −196 °C using a backscattering geometry. Excitation at 647.1 nm was provided by a Spectra-Physics BeamLok 2060-KR-V Krypton ion laser. Excitation at 514.5 nm was provided by a Spectra-Physics BeamLok 2065-7S argon ion laser. Raman shifts were externally referenced to indene and internally referenced to the solvent (THF).

X-ray Crystallographic and Structure Refinement Details. Single crystals of **1** were grown by adding hexamethyldisiloxane to a concentrated solution of **1** in Et_2O and storing at −30 °C. Brown plates of **1**, **2**, K(crypt-222)[3^{red}], and $4^{ox}[B(Ar_F)_4]$ and a green plate of K[2^{red}] were placed on the tip of a 0.1-mm-diameter glass capillary and mounted on a Bruker APEX II CCD diffractometer for data collection at 173(2) K for **1**, **2**, K[2^{red}], and K(crypt-222)[3^{red}] and at 123(2) K for $4^{ox}[B(Ar_F)_4]$. The data collection was carried out using Mo Kα radiation (graphite-monochromated). The data intensity was corrected for absorption and decay (SADABS).[17] Final cell constants were obtained from least-squares fits of all measured reflections. The structure was solved using SHELXS-97 and refined using SHELXL-97.[18] A direct-methods solution was calculated that provided most non-hydrogen atoms from the electron-density map (E map). Full-matrix least-squares/difference Fourier cycles were performed to locate the remaining non-hydrogen atoms. All non-hydrogen atoms were refined with anisotropic displacement parameters. Hydrogen atoms were placed in ideal positions and refined as riding atoms with relative isotropic displacement parameters. Complex **2** was solved in the space group $P321$ and contained channels along the crystallographic c axis; although substantial electron density was observed, no solvent molecules could be located. The SQUEEZE function of the PLATON program was used to remove solvent molecules within the void space.[19] The SQUEEZE function removed 839 electrons from a void-space volume of 396 Å^3. These values are consistent with the presence of approximately 21 THF molecules within the channel. Independent crystals of $4^{ox}[B(Ar_F)_4]$ displayed substantial disorder at 173 and 123 K. At 123 K, the entire cationic component was found to be

DOI: 10.1021/acs.inorgchem.5b01163
Inorg. Chem. 2015, 54, 7579−7592

disordered over two sites with a 57:43 occupancy. The anionic component exhibited rotational disorder of the CF_3 groups, which were treated as ideal rotors. One aryl ring of the counteranion appeared to exhibit rotational disorder, precluding anisotropic refinement of the respective CF_3 group. The presumed minor component of this disorder was not located during refinement. The data for $\mathbf{3}^{red}$ was twinned, and the appropriate twin law was applied. Crystallographic data are summarized in Table 1.

Computational Methods. A quantum chemical study of the model complexes, **2′**, $\mathbf{2}^{red\prime}$, $\mathbf{3}^{red\prime}$, and $\mathbf{4}^{ox\prime}$, was performed, where the isopropyl groups were truncated to methyl groups. Analogous studies for **3′**, **4′**, and $\mathbf{4}^{red\prime}$ were reported previously.[10] Gas-phase geometry optimizations were performed with density functional theory (DFT) using the Perdew–Burke–Ernzerhof (PBE) exchange-correlation functional as implemented in the TURBOMOLE 6.4 package.[20] Initial starting structures for geometry optimizations were derived from experimentally determined X-ray structures. No symmetry constraints were used. For C and H atoms, the double-ζ-quality basis set def-SV(P) was used. The triple-ζ-quality basis set def-TZVP was employed for N and P. Additional polarized functions were introduced for Fe, Mn, and Cr by using def-TZVPP.[21] The DFT calculations were performed using an unrestricted, broken-symmetry formalism, and the resolution of the identity (RI) approximation was used for the Coulomb integrals.[22] All stationary points were confirmed as minima by computing vibrational frequencies using the harmonic approximation. For $\mathbf{2}^{red\prime}$, Raman intensities were computed from polarizabilities as implemented in TURBOMOLE. To increase the accuracy of computed vibrational frequencies, a scale factor is commonly employed.[23] In the computed Raman spectra for $\mathbf{2}^{red\prime}$, the computed frequencies (391, 473, 503, 597 cm^{-1}) were scaled by a factor of 0.88 to obtain the reported frequencies (344, 416, 443, 524 cm^{-1}; Figure 10), whose intensities were plotted as a convolution of Lorentzian functions with half height widths of 10 cm^{-1}.

In addition to DFT calculations, the electronic structure was further investigated using complete-active-space and restricted-active-space self-consistent field (CASSCF/RASSCF) followed by second-order perturbation theory (CASPT2/RASPT2) calculations on the DFT/PBE-optimized geometries using the MOLCAS 7.8 package.[24] Relativistic effects were included through the use of the scalar Douglas–Kroll–Hess (DKH) Hamiltonian.[25] The relativistic all-electron ANO-RCC basis sets were used for all elements.[26] In all of these calculations, the ANO-RCC-VTZP basis set was used for Fe, Mn, and Cr; the ANO-RCC-VDZP basis set was used for N and P; and the ANO-RCC-MB basis set was used for C and H.[26] Additionally, the Cholesky decomposition technique was used combined with local exchange screening to reduce significantly the computational costs involved in generating the two-electron integrals.[27] Atomic charges were computed at the CASSCF level for the ground state using the LoProp procedure.[28]

Active-Space Choice. Previously, the CASSCF active space for **3′**, **4′**, and $\mathbf{4}^{red\prime}$ was constrained to the valence 3d electrons in 15 orbitals, including all of the 3d orbitals from the two metals and five empty correlating 4d orbitals of Mn or Fe.[10] A larger active space was used here for **2′**, $\mathbf{2}^{red\prime}$, $\mathbf{3}^{red\prime}$, and $\mathbf{4}^{ox\prime}$, consisting of the valence 3d electrons in 20 orbitals, including all of the 3d orbitals and empty correlating 4d orbitals of both metals. For consistency, **3′**, **4′**, and $\mathbf{4}^{red\prime}$ were recomputed with the larger active space, and the results were consistent with those of the earlier studies. To account for the double-shell effect, RASSCF calculations incorporating a large configuration interaction space were performed for all species and spin multiplicities, denoted by $(n,20)/(n,10)/2$, where n = 9, 10, and 11 for the $(d-d)^9$, $(d-d)^{10}$, and $(d-d)^{11}$ species, respectively.[5c] In this notation, the numbers in the first set of parentheses correspond to the total number of electrons (n) and the total number of orbitals (20) in all of the RAS spaces. The numbers in the second set of parentheses correspond to the number of active electrons and the number of orbitals in the primary space, containing the 3d orbitals of both metals. The final value of 2 refers to the maximum number of electrons allowed into the secondary space. The natural orbital occupation numbers were used for the evaluation of effective bond orders (EBOs), which were calculated as the difference between the total occupancies of the bonding and antibonding molecular orbitals of the metal–metal bond divided by 2.[5a,b]

State-averaged complete-active-space self-consistent field (SA-CASSCF) calculations were performed for the $(d-d)^{10}$ complexes. Because of the computational cost of calculating multiple electronic states, the active spaces for SA-CASSCF calculations were truncated from the aforementioned RASSCF choices to a (10,10) active space. For each $(d-d)^{10}$ complex, a six-root calculation was performed. The complete-active-space state interaction (CASSI) method was applied to compute the transition probabilities.[29] The CASSCF wave functions were employed together with the CASPT2 energies. CASSI results served to obtain a qualitative orbital ordering based on an analysis of the energies and natures of the orbitals involved in the electronic excitations of the various roots and to characterize the low-energy vis–NIR spectroscopic transitions.

RESULTS AND DISCUSSION

Synthesis and Cyclic Voltammetry (CV). The neutral MCr complexes for M = Mn and Fe were generated previously by mixing the metal dibromide precursors, MBr_2, with the monometallic chromium complex (**1**, CrL) and 2 equiv of reductant, KC_8 (Scheme 1).[10,30] A similar procedure was used

Scheme 1. Syntheses from Complex 1 (Left) of Neutral Metal–Chromium Complexes 2–4 and Their One-Electron-Reduced and/or -Oxidized Counterparts

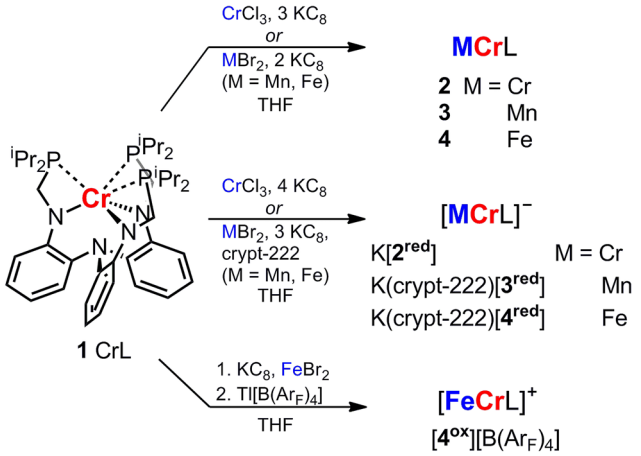

to generate the chromium homobimetallic complex. Mixing **1**, chromium(III) chloride, and 3 equiv of KC_8 produced the red-brown dichromium complex (**2**, Cr_2L). As previously reported, neutral MCr complexes with M = Mn, Fe, Co and Ni exhibit multiple one-electron-transfer processes by cyclic voltammetry (CV). The cyclic voltammogram of **2** is shown in Figure 2, along with the cyclic voltammograms of the manganese–chromium (**3**, MnCrL) and iron–chromium (**4**, FeCrL) complexes, and the redox potentials are listed in Table 2. Complex **2** exhibits two reversible, one-electron-transfer processes: an oxidation at −1.60 V and a reduction at −2.26 V (vs $FeCp_2/FeCp_2^+$). Presumably, reduction of **2** generates a $\{Cr_2\}^{10}$ species that would be isoelectronic to diamagnetic **3**. Collectively, the cyclic voltammograms suggest the possibility of characterizing several redox members (Figure 1), including an isoelectronic $(d-d)^{10}$ subset that comprises $[Cr_2L]^-$, MnCrL, and $[FeCrL]^+$.

The reduction of **4** to $[FeCrL]^-$ ($\mathbf{4}^{red}$) was previously achieved using 1 equiv of KC_8 in THF.[10b] The monoanionic counterparts of **2** and **3**, $[Cr_2L]^-$ ($\mathbf{2}^{red}$) and $[MnCrL]^-$ ($\mathbf{3}^{red}$),

DOI: 10.1021/acs.inorgchem.5b01163
Inorg. Chem. 2015, 54, 7579–7592

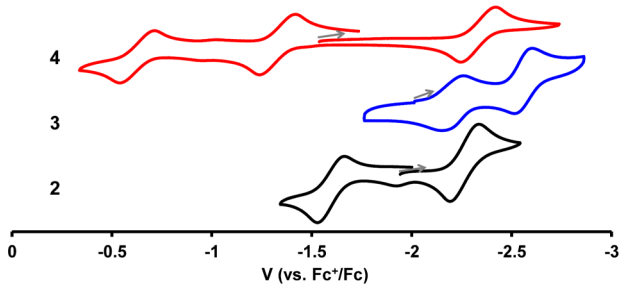

Figure 2. Cyclic voltammograms of **2**–**4** with $[^nBu_4N]PF_6$ (0.1–0.4 M) in THF (vs $FeCp_2^{0/+}$). Scan rates and electrolyte concentrations were as follows: **2** (black), 25 mV/s, 0.4 M; **3** (blue), 250 mV/s, 0.4 M; and **4** (red), 10 mV/s, 0.1 M.

Table 2. Redox Potentials[a] ($E°'$, V) of 2–4

complex	reduction	oxidation
2	−2.26	−1.60
3	−2.21, −2.55[b]	−1.18[c]
4	−2.33	−1.32, −0.62

[a]Versus $FeCp_2^{0/+}$. [b]Quasireversible. [c]Irreversible; E_{pa} reported.

respectively, were generated directly from **1** using $CrCl_3$ and $MnBr_2$, respectively, and the appropriate number of equivalents of KC_8 (Scheme 1). In THF, the color of $\mathbf{2}^{red}$ is forest-green, whereas $\mathbf{3}^{red}$ and $\mathbf{4}^{red}$ are red-brown. One equivalent of crypt-222 was added to solutions of $\mathbf{3}^{red}$ and $\mathbf{4}^{red}$ to improve the crystallinity of the salt product. Chemical oxidation of **4** to $[FeCrL]^+$ ($\mathbf{4}^{ox}$) can be performed with $[FeCp_2][B(Ar_F)_4]$. However, an alternative, cleaner synthesis of $[\mathbf{4}^{ox}][B(Ar_F)_4]$ avoids neutral **4** altogether. Complex **1** was stirred with 1 equiv KC_8 and then $FeBr_2$ to generate a green intermediate, which is presumably (Br)FeCrL. Abstraction of the halide with $Tl[B(Ar_F)_4]$ gave $[\mathbf{4}^{ox}][B(Ar_F)_4]$ in moderate yield. The presence of the $[B(Ar_F)_4]$ counterion renders $[\mathbf{4}^{ox}][B(Ar_F)_4]$ highly soluble even in hydrocarbon solvents such as benzene. So far, efforts to isolate the dicationic $(d-d)^9$ $[FeCrL]^{2+}$ or the dianionic $(d-d)^{12}$ $[MnCrL]^{2-}$ have not been fruitful.

NMR and EPR Spectroscopies. The three $(d-d)^{10}$ species $\mathbf{2}^{red}$, **3**, and $\mathbf{4}^{ox}$ are all diamagnetic, allowing for detailed comparisons by ^1H NMR spectroscopy. These complexes all display fluxional behavior, as shown in Figure 3 for $\mathbf{2}^{red}$ (for **3** and $\mathbf{4}^{ox}$, see Figures S6 and S9, respectively, SI). At high temperature, each complex exhibits C_{3v} symmetry (total of seven unique protons) with equivalent methyl, methylene, and methine protons. As the temperature is lowered, the solution structures of the MCrL species adopt a C_3-propeller configuration (total of 12 unique protons), where the methylene protons are diastereotopic and the two methine protons and four methyl groups are also distinct.

The energy barrier ($\Delta G^{\ddagger}$) for the fluxional process can be estimated from the coalescence temperature of the methylene peaks for the trio of $(d-d)^{10}$ complexes $\mathbf{2}^{red}$, **3**, and $\mathbf{4}^{ox}$.[16] For example, the coalescence of the methylene resonances of $\mathbf{2}^{red}$ occurs at 15 °C, as shown in Figure 3. The energy barriers for $\mathbf{2}^{red}$, **3**, and $\mathbf{4}^{ox}$ were estimated to be 13.0, 14.6, and 16.6 kcal mol^{-1}, respectively (Table S1, SI). Two possible mechanisms could account for the observed fluxionality: (1) dissociation of one phosphine donor followed by rotation and reassociation[31] or (2) a simple twisting of the methylene backbone while the phosphine arms remain associated. Unfortunately, the variable-temperature (VT) ^{31}P NMR behavior of these species (Figures S4, S7, and S10, SI) was inconclusive. Notably, the aryl protons of the ligand backbone remained sharp and coupled throughout the VT-NMR studies of $\mathbf{2}^{red}$, **3**, and $\mathbf{4}^{ox}$ (up to 60 °C), which rules out the presence of a low-lying triplet state (Figures S3, S6, and S9, SI).

The ^1H NMR spectrum of **2** is paramagnetic and displays 12 resonances, suggesting that it is locked in a C_3 environment on the NMR time scale (Figure S2, SI). The $S = {}^1/_2$ spin state was confirmed by X-band EPR spectroscopy (Figure 4a). The $S = {}^1/_2$ EPR signal is isotropic, with $g = 1.99$, which is typical for a Cr-based spin.[32] The spectral splitting arises from coupling to

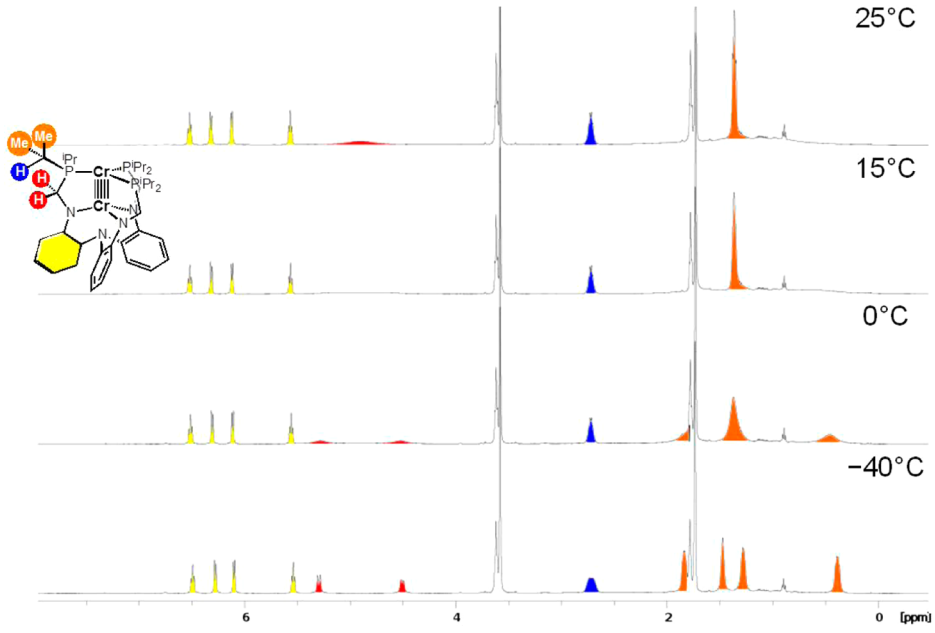

Figure 3. Stacked plot of variable-temperature ^1H NMR spectra for $K[\mathbf{2}^{red}]$ (THF-d_8, 500 MHz). Protons are color-matched to the inset color figure. For clarity, only one ligand arm is labeled.

DOI: 10.1021/acs.inorgchem.5b01163
Inorg. Chem. 2015, 54, 7579–7592

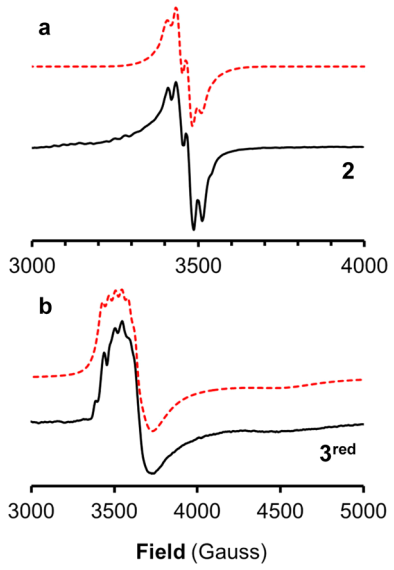

Figure 4. X-band EPR spectra (9.65 MHz) of (a) **2** (20 K) and (b) $\mathbf{3}^{red}$ (34 K) in frozen THF (1 mM). Experimental spectra are shown in solid black lines, with corresponding simulations in dashed red lines. Simulation parameters were as follows: for **2**, $g_x = g_y = g_z = 1.99$; W = (11, 16, 11 G), $A(3 \times {}^{31}P) = 10 \times 10^{-4}$ cm^{-1}; for $\mathbf{3}^{red}$, $g_{ave} = 1.79$, g = (1.95, 1.88, 1.52), W = (30, 200, 620) G, $A_x({}^{55}Mn) = 36 \times 10^{-4}$ cm^{-1}.

three $I = {}^1/_2$ ^{31}P nuclei with an isotropic coupling constant (A) of 10×10^{-4} cm^{-1}, suggesting that spin density resides at the Cr center in the phosphine-binding pocket. Notably, the hyperfine coupling is lower than that reported for octahedral phosphine-ligated Cr(I) carbonyls, such as $[Cr(CO)_3(PMe_3)_3]^+$, which feature hyperfine coupling constants in the range of 57–96 MHz, or $(19–36) \times 10^{-4}$ cm^{-1}.[33] This might suggest some delocalization of the unpaired spin in dichromium unit. Complex $\mathbf{3}^{red}$ is also paramagnetic, and the 10 resonances observed by ^{1}H NMR spectroscopy are consistent with C_3 symmetry (Figure S12, SI). The solution-state magnetic moment of $\mathbf{3}^{red}$ is 1.87 μ_B, indicating $S = {}^1/_2$.[34] The X-band EPR spectrum of $\mathbf{3}^{red}$ (Figure 4, bottom) is rhombic, with g = (1.95, 1.88, 1.52), where g_{ave} is 1.79. Hyperfine coupling to the ^{55}Mn nucleus ($I = 5/2$) can be discerned in g_x where $A_x = 36 \times 10^{-4}$ cm^{-1}. Complex **4**, with a (d–d)[11] electron count, was previously characterized as $S = {}^1/_2$ by EPR spectroscopy. The reported g_{ave} value of 1.88 for complex **4** is consistent with a Cr-based spin.

Solid-State Structures. Single-crystal X-ray diffraction studies of complexes **1**, **2**, $\mathbf{2}^{red}$, $\mathbf{3}^{red}$, and $\mathbf{4}^{ox}$ provided the solid-state structures shown in Figure 5, with the relevant geometric parameters in Table 3. For comparison, the data for previously reported compounds **3** and **4** are also included. All of the complexes are essentially threefold-symmetric and have a highly conserved coordination geometry. As anticipated based on our previous work, **2**, $\mathbf{2}^{red}$, $\mathbf{3}^{red}$, and $\mathbf{4}^{ox}$ all have ultrashort metal–metal bonds (<2.0 Å), suggesting multiply bonded metal atoms. Dichromium complex $\mathbf{2}^{red}$ has the shortest metal–metal bond distance in the series, at 1.7407(6) Å, as well as one of the shortest dichromium distances in the literature (Table 4).[6a,35] Among heterometallic complexes, the shortest metal–metal bonds are currently found in **3** and $\mathbf{3}^{red}$, followed by the (d–d)[10–12] FeCr complexes $\mathbf{4}^{ox}$, **4**, and $\mathbf{4}^{red}$ [10b] and the (d–d)[9,10] FeV complexes $V(^iPrNPPh_2)_3FeI$ and $V(^iPrNPPh_2)_3FePMe_3$.[9c]

As an aside, all of the examples cited above use bridging ligand(s) to stabilize the bimetallic cores. A long-standing critique has been that the bridging ligands might ultimately be responsible for short metal–metal distances, in lieu of any true metal–metal bonding. It then follows that the diamagnetic (or low-spin) nature of the bimetallic species arises from antiferromagnetic coupling of the two metal spins. We would argue that this critique is invalid here. The present ligand is highly flexible and supports a wide range of metal–metal distances, not all of which are short. For example, the isostructural CoCrL and NiCrL complexes have longer M—Cr bond distances of 2.14 and 2.41 Å, respectively. Indeed, the M—Cr bond lengths change by 0.7 Å from $[Cr_2L]^-$ ($\mathbf{2}^{red}$) to NiCrL, which is substantially larger than any intrinsic differences in the metals' single-bond metallic radii (Cr, 1.172 Å; Ni, 1.149 Å) or covalent radii (Cr, 1.39 Å; Ni, 1.24 Å).[36] Also, despite a constant ligand and supporting Cr metal, the Cr—N_{apical} bond length changes by 0.4 Å (2.50 Å in $\mathbf{2}^{red}$, 2.09 Å in NiCrL). Finally, an absence of metal–metal interaction would require the two metal-based spins to couple antiferromagnetically, either through the ligand or through space. The former cannot account for singlet–triplet splitting of more than 10–100 cm^{-1} because the ligand backbone is saturated, where fully diamagnetic behavior at room temperature requires excited spin states to be higher than 1000 cm^{-1} in energy. Spin–spin interactions through space are even weaker (ca. 1

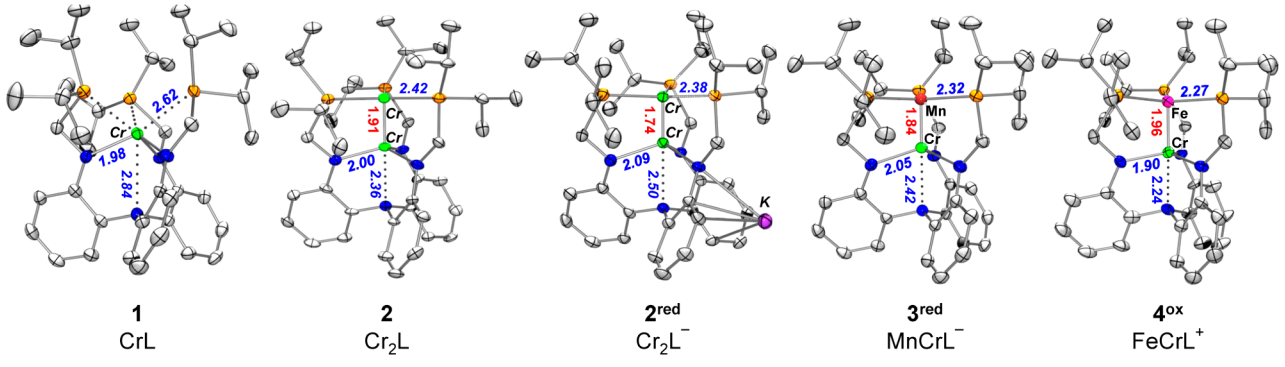

Figure 5. Solid-state structures of **1**, **2**, $\mathbf{2}^{red}$, $\mathbf{3}^{red}$, and $\mathbf{4}^{ox}$ obtained by X-ray crystallography at 123 K for $\mathbf{4}^{ox}$ and at 173 K for the remaining compounds. Thermal ellipsoids are shown at 50% probability. Hydrogen atoms, counterions, and lattice solvent molecules have been omitted for clarity. Green, chromium; red, manganese; pink, iron; blue, nitrogen; orange, phosphorus. M—Cr bond distances are given in red, and average M—P and Cr—N bond distances are given in blue.

DOI: 10.1021/acs.inorgchem.5b01163
Inorg. Chem. 2015, 54, 7579–7592

Table 3. Geometrical Parameters, Including Bond Lengths (Å) and Angles (deg), for 2−4[a]

	2	2^{red}	3	3^{red}	4	4^{ox}
M—Cr (Å)	1.913(1)	1.7407(6)	1.8192(9)	1.8389(6)	1.944(1)	1.955(7)
r^b	0.82	0.74	0.78	0.79	0.83	0.84
M—P (Å)	2.420(1)	2.3844(9) ± 0.004	2.3792(7)	2.3167(5)	2.265(2) ± 0.004	2.268(8) ± 0.014
Cr—N_{eq} (Å)	1.997(3)	2.094(2) ± 0.014	2.010(3)	2.0472(15)	1.960(2) ± 0.019	1.889(8) ± 0.011
Cr—N_{ap} (Å)	2.359(5)	2.499	2.370(3)	2.416(2)	2.284(3)	2.240(9)
M to P_3 plane (Å)	−0.132	−0.203	−0.189	−0.174	−0.192	−0.270
Cr to N_3 plane (Å)	+0.447	+0.654	+0.494	+0.558	+0.412	+0.329
∑(P—M—P) (deg)	359.12	357.85	358.14	358.32	357.85	355.9
∑(N—Cr—N) (deg)	345.45	332.09	342.51	338.49	347.1	351.1
M—Cr—N_{ap} (deg)	180	179.85	180	180	177.5	178.1

[a]Complexes 2^{red}, 4, and 4^{ox} crystallized with approximate threefold symmetry, so several parameters (e.g., M—P bond lengths) represent the averages of three (2^{red}) or six (4) distinct values. Estimated standard deviations (esd) are provided in parentheses, and standard deviations of averages are shown with ± after the average value. [b]r = ratio of the M—Cr bond distance to the sum of the M and Cr single-bond metallic radii.[36a]

Table 4. Ultrashort Cr—Cr Bond Distances in Selected Cr_2 Systems

Cr_2 complex	d(Cr—Cr) (Å)	r	ref(s)
Cr_2(2,6-(2,6-^{i}Pr$_2$C$_6$H$_3$)$_2$C$_6$H$_3$)$_2$	1.8351(4)	0.78	6a
Cr_2(2,6-(2,6-^{i}Pr$_2$C$_6$H$_3$)$_2$-4-SiMe$_3$(C$_6$H$_2$))$_2$	1.8077(7)	0.77	35a
Cr_2(*N*,*N*′-bis(2,6-diisopropylphenyl)-1,4-diazadiene)$_2$	1.8028(9)	0.77	35e
K[Cr_2L] (2^{red})	1.7407(6)	0.74	this work
Cr_2(HC(N(2,4,6-(CH$_3$)$_3$C$_6$H$_2$)$_2$)$_2$	1.7404(8)	0.74	35f
K(crypt-222)[Cr_2(HC(N(2,6-(CH$_3$)$_2$C$_6$H$_3$)$_2$)$_3$]	1.7397(9)	0.74	35g, 38
Cr_2(Me$_2$NC(N(2,6-^{i}Pr$_2$C$_6$H$_3$)$_2$)$_2$	1.7293(12)	0.74	35c
Cr_2((2,6-(CH$_3$)$_2$C$_5$H$_8$N)C(2,6-^{i}Pr$_2$C$_6$H$_3$)$_2$)$_2$	1.7056(12)	0.73	35d
Cr_2^{-} [a]	1.705(10)[b]	0.73	39
Cr_2 [a]	1.68(1)[b]	0.72	40

[a]Gas phase. [b]Based on a Morse fit of the vibrational frequency or rotational analysis.

cm^{-1}), even at a short distance of 1.5 Å.[37] Thus, the argument for through space spin−spin coupling is highly inconsistent with the fully diamagnetic behavior of 2^{red}, 3, and 4^{ox} in the VT-NMR studies described above.

A useful metric for comparing metal−metal bonding across different metals is the formal shortness ratio (r),[41] which is defined as the ratio of the metal−metal bond distance to the sum of the single-bond metallic radii.[36a] By accounting for the sizes of different metals, the r value allows for a more fair comparison between homo- and heterobimetallic bonds. As defined, values close to unity represent single bonds, and values significantly below unity indicate multiple bonds. The r values for all complexes here are well below unity (0.74−0.84). The isoelectronic species $\{Cr_2\}^{10}$ 2^{red} and $\{MnCr\}^{10}$ 3 have the lowest r values of 0.74 and 0.78, respectively. We propose these low r values are indicative of delta bonding, and theoretical studies support these molecules as being fomally quintuply bonded ($\sigma + 2\pi + 2\delta$).[10a] We have also shown that the δ-symmetry d orbitals at iron and chromium in $\{FeCr\}^{11}$ 4 do not interact because of their poor energy overlap, and hence, the formal bond order decreases to 3 ($\sigma + 2\pi$). Because 4^{ox} has an r value that is close to that of 4, 4^{ox} is also interpreted as triply bonded. Indeed, 4^{ox} is characterized by the largest r value in this series, 0.84, consistent with its lower bond order. According to the r values, $\{Cr_2\}^9$ 2 and $\{MnCr\}^{11}$ 3^{red} are in the middle of this series, suggesting an intermediate bond order between 3 and 5. For $(d-d)^9$ and $(d-d)^{11}$ systems, the expected dominant electronic configurations of $(\sigma)^2(\pi)^4(\delta)^3$ and $(\sigma)^2(\pi)^4(\delta)^4(\delta^*)^1$, respectively, would both predict a bond order of 4.5. However, the r value for 2 is only slightly lower than those for the Fe—Cr triply bonded complexes 4 and 4^{ox}. A possible explanation is that the two δ bonds are not fully formed in the case of 2, resulting in a bond order less than 4.5 (vide infra). The Cr—Cr bond distance of 1.913(1) Å in 2 is consistent with a wide range of dichromium complexes with formal quadruple bonds.[41] Also, δ bonds are weak by nature, so their effects on bond lengths (and r values) are often unclear.[42]

X-ray crystallography can sometimes be useful to reveal changes in metal oxidation states through corresponding changes in metal−ligand bond lengths. Structural comparison between various redox states might provide insight into the redox site(s), although these are preliminary assignments, as d electrons can easily delocalize across the two metals, and they should be validated with complementary spectroscopic and theoretical studies. The metal−metal bond contracts substantially between $\{Cr_2\}^9$ 2 and $\{Cr_2\}^{10}$ 2^{red} (Δ = −0.17 Å), which is about twice the change observed in the analogous redox pair $[Cr_2(ArNC(H)NAr)_3]^{0/-}$ [Δ = −0.08 Å, Ar = 2,6-(CH$_3$)$_2$C$_6$H$_3$].[38] One possible explanation for the relatively long Cr—Cr interaction in 2 versus 2^{red} is the variable strength of the Cr—N_{apical} interaction, which lengthens appreciably upon reduction (Δ = 0.14 Å). The presence of axial donors is well-known to elongate Cr—Cr multiple bonds, and σ donors can account for changes up to 0.1 Å.[41,43] Reduction of 2 to 2^{red} also induces contraction of Cr—P bond distances and elongation of Cr—N_{eq} bond distances by 0.036 and 0.097 Å, respectively. The greater change in the Cr—N_{eq} bond distances might suggest a more localized reduction at the Cr residing in the amide-binding pocket.

Upon reduction of the formally quintuply bonded $\{MnCr\}^{10}$ 3 to $\{MnCr\}^{11}$ 3^{red}, the metal−metal bond lengthens slightly from 1.8192(9) to 1.8389(6) Å, which is expected as the

DOI: 10.1021/acs.inorgchem.5b01163
Inorg. Chem. 2015, 54, 7579−7592

additional electron should populate an antibonding orbital. Upon reduction, the Mn—P bond distances decrease (Δ = −0.063 Å), whereas the Cr—N distances increase [Δ(Cr—N_{eq}) = 0.037 Å, Δ(Cr—N_{ap}) = 0.046 Å], which can be interpreted as stronger manganese−phosphine back-bonding and increased Cr—N_{eq} repulsion upon reduction of the MnCr core. In contrast, the oxidation of **4** did not produce any statistically significant changes in the Fe—Cr and Fe—P bond metrics, but alterations in the Cr—N_{eq} bond were statistically significant [Δ = 0.07(2) Å]. These structural changes possibly suggest oxidation at Cr, but we note that the esd values in $\mathbf{4}^{ox}$ (up to 0.009 Å) are large enough to mask moderate changes.

Diamagnetic Anisotropy. In analogy with unsaturated organic molecules with π bonds, complexes with multiple metal−metal bonds can have large diamagnetic anisotropies, Δχ, that impact their NMR chemical shifts.[44] In axially symmetric molecules, the circulating electrons in the multiple bond can either shield (+) or deshield (−) nearby protons, depending on the proton's position within the spatial zones demarcated by the double cone, as shown in Figure 6. Protons

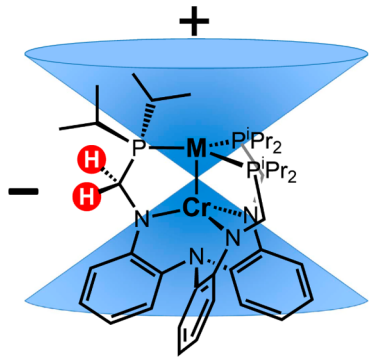

Figure 6. Spatial zones of shielded (+) and deshielded (−) chemical shifts that arise from the diamagnetic anisotropy of the multiply bonded $\{MCr\}^{10}$ cores.

in the equatorial region, for example, methylene resonances, are expected to shift downfield if multiple bonds are present. Indeed, the methylene protons in all three $(d-d)^{10}$ complexes (**3**, $\mathbf{2}^{red}$, and $\mathbf{4}^{ox}$) are significantly deshielded, appearing 2−3 ppm downfield relative to the methylene protons in the free ligand.[45] The diamagnetic anisotropy ($\chi_{\parallel} - \chi_{\perp}$or Δχ) can be calculated using the equation[15]

$$\Delta\delta = \left(\frac{1}{3r^3}\right)\frac{(\chi_{\parallel} - \chi_{\perp})[1 - 3\cos^2(\theta)]}{4\pi}$$

where Δδ is the difference in ^{1}H NMR chemical shifts of the methylene protons in the multiply bonded bimetallic complex compared to that of a reference complex without any multiple metal−metal bonds. For the reference complex, we chose the isostructural Ni−Al bimetallic featuring a Ni → Al dative bond (Figures S14 and S15, SI).[11] The remaining variables were extracted from the corresponding solid-state structures: r is the distance and θ is the acute angle of the methylene protons relative to the center and axis of the metal−metal bond, respectively. By assimilating data from NMR and X-ray crystallographic studies, we implicitly assume that the solution and solid-state structures are similar. In addition, we discount an energetically low-lying triplet state as the cause of the dramatic NMR shifts. The VT-NMR profiles of $\mathbf{2}^{red}$, **3**, and $\mathbf{4}^{ox}$ are inconsistent with paramagnetic contributions (Figures S3, S6, and S9, SI). Moreover, in the dichromium species that have thermally accessible singlet−triplet gaps, the Cr—Cr bond distances are dramatically longer, ≥2.25 Å.[46]

Whereas diamagnetic anisotropies are known for several homobimetallic species, such data are limited for heterobimetallic pairings (Table 5).[44c,d,47] Cotton and co-workers

Table 5. Diamagnetic Anisotropies (Δχ) of Multiply Bonded Bimetallic Complexes

complex[a]	Δχ (×10^{-36} m^3 molecule^{-1})	ref
$\mathbf{2}^{red}$	−3500	this work
3	−3900	this work
$\mathbf{4}^{ox}$	−5800	this work
$Cr_2(DFM)_4$	−5230	47b
$Mo_2(DFM)_4$	−5020	47b[b]
$W_2(DFM)_4$	−5480	47b
$Re_2(DFM)_4$	−4430	47b[b]
$Ru_2(DFM)_4$	−3780	47b[b]
$Mo_2X_4(PP)_2$	−4450[c]	48
$MoWCl_4(PP)_2$	−5082[c]	47a
$W_2X_4(PP)_2$	−5727[c]	47c

[a]DFM = di-*p*-tolylformamidinate; PP = dppe, dppm, dmpm, dmpe. [b]And references therein. [c]Average value.

systematically studied a series of quadruply bonded complexes, $M_2X_4(\mu\text{-}PP)_2$, where M_2 = Mo_2, MoW, and W_2.[47a,c,48] The average Δχ values were found to increase across the pairings in the order Mo_2 < MoW < W_2, where each substitution of a Mo center for W increased Δχ by approximately −640 × 10^{-36} m^3 molecule^{-1} (13%). The Δχ values calculated for $\{Cr_2\}^{10}$ $\mathbf{2}^{red}$, $\{MnCr\}^{10}$ **3**, and $\{FeCr\}^{10}$ $\mathbf{4}^{ox}$ in this work are −3500 × 10^{-36}, −3900 × 10^{-36}, and −5800 × 10^{-36} m^3 molecule^{-1}, respectively. The diamagnetic susceptibility should increase with the effective bond order, but polarization of the metal−metal bond can dominate. Substituting Mn for Cr results in an 11% gain in Δχ, whereas swapping Fe for Cr produces a dramatic 66% increase. This trend is well-known in organic molecules, whereby heteronuclear π bonds, such as C═O (+420) and N═O (+1300), exhibit larger diamagnetic anisotropies than their homonuclear analogues, in this case C═C (+150) and C≡C (−340), respectively.[49]

Theoretical Calculations. Quantum chemical studies were conducted on the bimetallic models **2′**, $\mathbf{2}^{red\prime}$, $\mathbf{3}^{red\prime}$, and $\mathbf{4}^{ox\prime}$, where the isopropyl groups were truncated to methyl groups. Computational studies of **3′** and **4′** were reported previously.[10] Geometry optimizations were performed using density functional theory (DFT) for several possible spin states. For all of the complexes, the computed spin state with the lowest energy corresponded to the proposed ground state backed by experimental evidence (Tables S4−S7, SI). To address the strong correlation effects known for complexes with metal−metal bonds, we performed complete-active-space self-consistent field (CASSCF) followed by second−order perturbation theory (CASPT2) calculations. These methods give a more accurate description of bimetallic systems that are characterized by a heavy multireference character, large dynamic correlation energy, and/or significant relativistic effects.[5a,50] For many of the systems in this work, a single electronic configuration represents the majority (55−64%) of the ground-state wave function. The exception is **2′**, for which the contribution of the main configuration is slightly lower at 42% (Table 6).

DOI: 10.1021/acs.inorgchem.5b01163
Inorg. Chem. 2015, 54, 7579−7592

Table 6. Main Electronic Configurations of Metal–Chromium Complexes and Formal versus Effective Bond Orders (FBOs vs EBOs)

MCr complex	main electronic configuration	%[a]	r^b	FBO	EBO
	$(d-d)^9$				
CrCr (**2′**)	$\sigma^2\pi^4\delta^2(Cr\ d_{xy})^1$	42	0.82	4	2.71
	$(d-d)^{10}$				
CrCr ($\mathbf{2}^{red\prime}$)	$\sigma^2\pi^4\delta^4$	60	0.74	5	3.99
MnCr (**3′**)	$\sigma^2\pi^4\delta^4$	55	0.78	5	3.85
FeCr ($\mathbf{4}^{ox\prime}$)	$\sigma^2\pi^4(Fe\ d_{xy}, d_{x^2-y^2})^4$	55	0.84	3	2.21
	$(d-d)^{11}$				
MnCr ($\mathbf{3}^{red\prime}$)	$\sigma^2\pi^4(Mn\ d_{xy}, d_{x^2-y^2})^4(Cr\ d_{xy})^1$	64	0.79	3	2.39
FeCr (**4′**)	$\sigma^2\pi^4(Fe\ d_{xy}, d_{x^2-y^2})^4(Cr\ d_{xy})^1$	58	0.83	3	2.15
	$(d-d)^{12}$				
FeCr ($\mathbf{4}^{red\prime}$)	$\sigma^2\pi^4(Fe\ d_{xy}, d_{x^2-y^2})^4(Cr\ d_{xy})^2$	60	0.84	3	2.35

[a]Percentage of the ground-state wave function that is described by the main configuration. [b]Formal shortness ratio (experimentally determined; see text for definition).

Because of the weak ligand field associated with trigonal coordination geometries, all five d orbitals in these bimetallic species have the potential to participate in metal–metal bonding. The d orbitals can combine maximally to form quintuple bonds comprising one σ (d_{z^2}), two π (d_{xz}, d_{yz}), and two δ (d_{xy}, $d_{x^2-y^2}$) bonds. Indeed, all five of these interactions are observed in $\mathbf{2}^{red\prime}$ and **3′**, where the $(d-d)^{10}$ electron count fills all of the metal–metal bonding molecular orbitals (MOs), as shown in Figure 7 for $\mathbf{2}^{red\prime}$. Such a high bond order is consistent with the exceedingly low r values of 0.74 and 0.78 determined from experiment for $\mathbf{2}^{red}$ and **3**, respectively.

However, this simple MO picture does not hold for the other members (Figures S23–S29, SI). In complexes where the two metal partners are increasingly different, e.g., Fe and Cr in $\mathbf{4}^{ox\prime}$, **4′**, and $\mathbf{4}^{red\prime}$, the metal–metal bonds are increasingly polarized, resulting in localization of the δ-symmetric d orbitals so that only delocalized σ and π bonds remain (Table 6). Indeed, an r value of 0.84 for $(d-d)^{10}$ $\mathbf{4}^{ox}$ is more congruous with threefold rather than fivefold bonding. Fivefold interactions also break down when the electron count deviates from $(d-d)^{10}$. In $(d-d)^9$ **2′** and $(d-d)^{11}$ $\mathbf{3}^{red\prime}$ and **4′**, one would predict FBOs of 4.5 based on the simple MO pictures. However, as one or both pairs of δ-symmetric d orbitals become increasingly localized (Table 7), the formal bond orders drop to 4, 3, and 3 for **2′**, $\mathbf{3}^{red\prime}$, and **4′**, respectively.

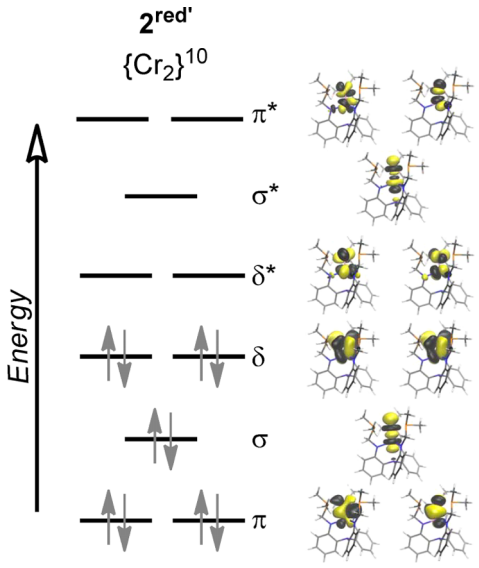

Figure 7. Qualitative MO diagram of $\mathbf{2}^{red\prime}$ showing the natural bonding orbitals of σ (d_{z^2}), π (d_{xz}, d_{yz}), and δ (d_{xy}, $d_{x^2-y^2}$) symmetry for the main configuration (60%) from RASSCF calculations.

Table 7. Percentages of Metal Character (%Cr, %M) in Metal–Chromium Bonding Orbitals of σ, π, and δ Symmetries from CASSCF Calculations

	σ		π		δ[a]	
MCr complex	%Cr	%M	%Cr	%M	%Cr	%M
			$(d-d)^9$			
CrCr (**2′**)	46	54	52	48	50	50
			52	48	*0*	*100*
			$(d-d)^{10}$			
CrCr ($\mathbf{2}^{red\prime}$)	45	55	48	52	39	61
			48	52	39	61
MnCr (**3′**)	40	60	38	62	33	*67*
			38	62	33	*67*
FeCr ($\mathbf{4}^{ox\prime}$)	33	*67*	45	54	*13*	*87*
			44	56	*12*	*88*
			$(d-d)^{11}$			
MnCr ($\mathbf{3}^{red\prime}$)	44	56	47	53	*14*	*86*
			53	47	*3*	*97*
FeCr (**4′**)	31	*69*	45	55	*8*	*92*
			49	51	*18*	*82*
			$(d-d)^{12}$			
FeCr ($\mathbf{4}^{red\prime}$)	36	*64*	27	73	*0*	*100*
			27	73	*0*	*100*

[a]Italicized values are percentages below 75%/25% and represent δ-bonding MOs that are more aptly described as localized, e.g., d_{xy}.

Whereas the formal bond order (FBO) is based solely on a single main configuration, the effective bond order (EBO) takes into account the natural populations of bonding/antibonding orbitals summed over *all* contributing configurations (Table 6). The quintuply bonded species $\mathbf{2}^{red\prime}$ and **3′** have EBO values that are closer to quadruple bonds. This is not unusual, as other quintuply bonded dichromium complexes in the literature also have EBOs close to 4.[6a,35c,d,f,g,38,50a] The triply bonded species $\mathbf{3}^{red\prime}$, $\mathbf{4}^{ox\prime}$, **4′**, and $\mathbf{4}^{red\prime}$ have slightly lowered EBOs, ranging from 2.21 to 2.39. The formally quadruply bonded complex **2′** shows the steepest reduction of bond order, with an EBO of 2.71, which is a direct result of its more multiconfigurational nature and, hence, partial population of the higher-lying antibonding orbitals. Because the r value of 0.82 for **2** is on par with the values for the other triply bonded complexes, a lower bond order is reasonable.

An analysis that parses the natural population of the active-space orbitals into weighted contributions from each metal partner can provide the d-electron count at each metal center, which can be useful in contemplating oxidation states (Tables S9–S14, SI). In a first approximation of the neutral bimetallics, the asymmetric charge distribution in the ligand would favor a trivalent metal in the triamido pocket, for example, M_N(III), while stabilizing a zerovalent metal in the triphosphine site, for example, M_P(0). However, because of covalent metal–metal bonding, the electronic charges can be further distributed

DOI: 10.1021/acs.inorgchem.5b01163
Inorg. Chem. 2015, 54, 7579–7592

between the two metal centers. For neutral dichromium **2′** and MnCr **3′**, the calculated oxidation states are consistent with $M_P(I)M_N(II)$, specifically, $Cr_P(1.0)Cr_N(2.0)$ and $Mn(0.9)$-$Cr(2.1)$. Their one-electron reduced counterparts, $\mathbf{2}^{red\prime}$ and $\mathbf{3}^{red\prime}$, have core oxidation states of $Cr_P(0.5)Cr_N(1.5)$ and $Mn(0.3)Cr(1.7)$, respectively, where the additional electron is delocalized on the two metal partners nearly equally. The neutral FeCr complex **4′**, which has core oxidation states of $Fe(0.6)Cr(2.4)$, is halfway between the two extremes of $M_P(0)M_N(III)$ and $M_P(I)M_N(II)$. Its redox analogues $\mathbf{4}^{ox\prime}$, $Fe(1.2)Cr(2.8)$, and $\mathbf{4}^{red\prime}$, $Fe(0)Cr(2.0)$, are interpreted as containing Fe(I) and Fe(0), respectively. Thus, the computations predict that reduction of the $(FeCr)^n$ core is equally shared by the two metals, whereas oxidation is primarily localized at the iron site.

With the calculated structures in hand, we were also able to gauge the *predicted* structural perturbations upon change of redox state (Table S18, SI). Upon comparison of the neutral bimetallics against their charged analogues, it became clear that the predicted bond changes are all consistent with increased Cr—N repulsion (elongation) and increased M—P π-back-bonding (contraction) upon reduction. Notably, the Cr—N_{eq} and Cr—N_{ap} bonds are extremely sensitive, elongating by 0.05−0.07 and 0.03−0.09 Å, respectively, per additional electron. In contrast, the M—P bonds were fairly insensitive, decreasing by ≤0.02 Å per additional electron. For example, the differences between **4′** and $\mathbf{4}^{ox\prime}$, which were predicted to be primarily Fe-based, include a 0.05-Å change in the Cr—N_{eq} bond length, but as little as a 0.007-Å perturbation in the Fe—P bond.

Mössbauer Spectroscopy. To elucidate the redox changes at the iron site, $\mathbf{4}^{ox}$ was further investigated by ^{57}Fe Mössbauer spectroscopy (Figure 8). The Mössbauer doublet is characterized by an isomer shift of 0.18 mm/s and a quadrupole splitting (ΔE_Q) of +5.85 mm/s. Previously, **4** and two variants of $\mathbf{4}^{red}$ [with K(crypt-222) and K(18-c-6) counterions] were analyzed by Mössbauer spectroscopy. Akin to **4** and $\mathbf{4}^{red}$, $\mathbf{4}^{ox}$ has an excessively large ΔE_Q value (>5.0 mm/s), which was attributed to large charge anisotropy in the iron valence shell that arises from the strong covalent bonds within the $[FeCr]^{3+}$ core. Whereas **4** and $\mathbf{4}^{red}$ showed essentially identical isomer shifts of 0.25 and 0.26−0.29 mm/s, respectively,[10b] $\mathbf{4}^{ox}$ has a notably lower isomer shift by approximately 0.1 mm/s. Differences in isomer shifts are essentially determined by the degree of 4s-electron population at the Mössbauer atom, which arises from covalent-bond formation with σ-type ligand orbitals.[51] Higher oxidation states, at least for Werner-type complexes in the mid-to-high-valent regime, cause shorter iron ligand bonds and, hence, lower isomer shifts.[52] Hence, the oxidation state of the iron nucleus remains Fe(0) in **4** and $\mathbf{4}^{red}$, but increases to Fe(I) in $\mathbf{4}^{ox}$.

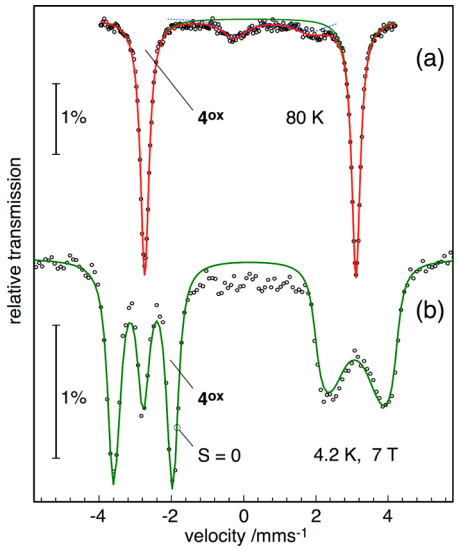

Figure 8. (a) Zero-field ^{57}Fe Mössbauer spectrum of $\mathbf{4}^{ox}$ recorded at 80 K and (b) magnetic spectrum recorded at 4.2 K with a field of 7 T applied perpendicular to the γ-rays. The green line represents the best fit with δ = 0.18 mm s^{-1}, ΔE_Q = +5.85 mm s^{-1}, η = 0 (85% purity), and S = 0. There is also a high-spin Fe(II) impurity with δ = 0.83 mm s^{-1} and ΔE_Q = 2.15 mm s^{-1} (dotted blue line in top panel).

However, one has to note that, in the low-valent regime [e.g, Fe(0), Fe(I)], the negative correlation of the isomer shift with the oxidation state typically fades, and even the opposite scenario can be observed, namely, that *lower* oxidation states result in *lower* isomer shifts.[53,54,9c] This has been explained by the onset of Fe(3d) → π-back-donation for low-valent iron,[55] which, by shortening the iron ligand bonds, leads to increased s-electron density at the Mössbauer nucleus, giving lower isomer shifts. In two representative redox series, $[(SiP_3)FeN_2]^n$ and $[(SiP_3)FeCO]^n$,[53] the Fe—P bond lengths contract by ca. 0.1 Å per unit oxidation state decrease from Fe(II) to Fe(0), which lends support to increased π-back-bonding from low-valent iron. In contrast, the FeCr series does not fit with other low-valent iron complexes. The average Fe—P bond distances in $\mathbf{4}^{ox}$, **4**, and $\mathbf{4}^{red}$ are all similar at 2.268(8), 2.265(2), and 2.2444(8) Å, respectively, and no Fe—P back-bonding is observed. The isomer shifts of **4** and $\mathbf{4}^{ox}$ behave as expected (for no Fe—L back-donation) and are consistent with the proposed oxidation states of Fe(0) and Fe(I), respectively.

Vis−NIR and Resonance Raman (rR) Spectroscopies. The electronic absorption spectra of the bimetallic complexes, as shown in Figure 9 and summarized in Table 8, were recorded in THF at room temperature. Except for a common UV peak at ∼310 nm, which is ascribed to a ligand-based transition, the MCr bimetallics show sufficiently different vis−NIR transitions that justify substantial metal-based character. Generally, in the electronic spectra of multiply bonded bimetallic complexes, the most interesting feature is the $\delta \rightarrow \delta^*$-type transition.[47b,56] A seminal study of quadruply bonded M_2^{4+} cores in tetragonal $M_2X_4P_4$ complexes revealed dramatic red shifts in the $\delta^2 \rightarrow \delta\delta^*$ energies upon metal substitution of W for Mo: Mo_2^{4+} (average 608 nm, 16460 cm^{-1}) > MoW^{4+} (658 nm, 15200 cm^{-1}) > W_2^{4+} (682 nm, 14660 cm^{-1}).[47c] The first heavy-metal substitution, namely, Mo_2^{4+} to MoW^{4+}, perturbs the $\delta^2 \rightarrow \delta\delta^*$ excitation significantly more than the second substitution, namely, MoW^{4+} to W_2^{4+}. Similar effects of metal substitution were also observed in a trio of homobimetallic $M_2(mhp)_4$ compounds (M_2 = Cr_2, Mo_2, W_2; mhp = deprotonated 6-methyl-2-hydroxypyridine), where the $\delta^2 \rightarrow \delta\delta^*$ energies decrease down the group (from 22500 cm^{-1} for M_2 = Cr_2 to 18700 cm^{-1} for M_2 = W_2).[56a] To our knowledge, electronic absorption data are limited for trigonal M_2^{n+} systems and especially so for quintuply bonded species.[6a,35a,e,f,57] Thus, we were keen to determine the $\delta^4 \rightarrow \delta^3\delta^*$ transition energy in the isoelectronic quintuply bonded complexes $\mathbf{2}^{red}$ and **3**, which would allow a quantitative comparison between homo- and heterobimetallic quintuple bonds.

DOI: 10.1021/acs.inorgchem.5b01163
Inorg. Chem. 2015, 54, 7579−7592

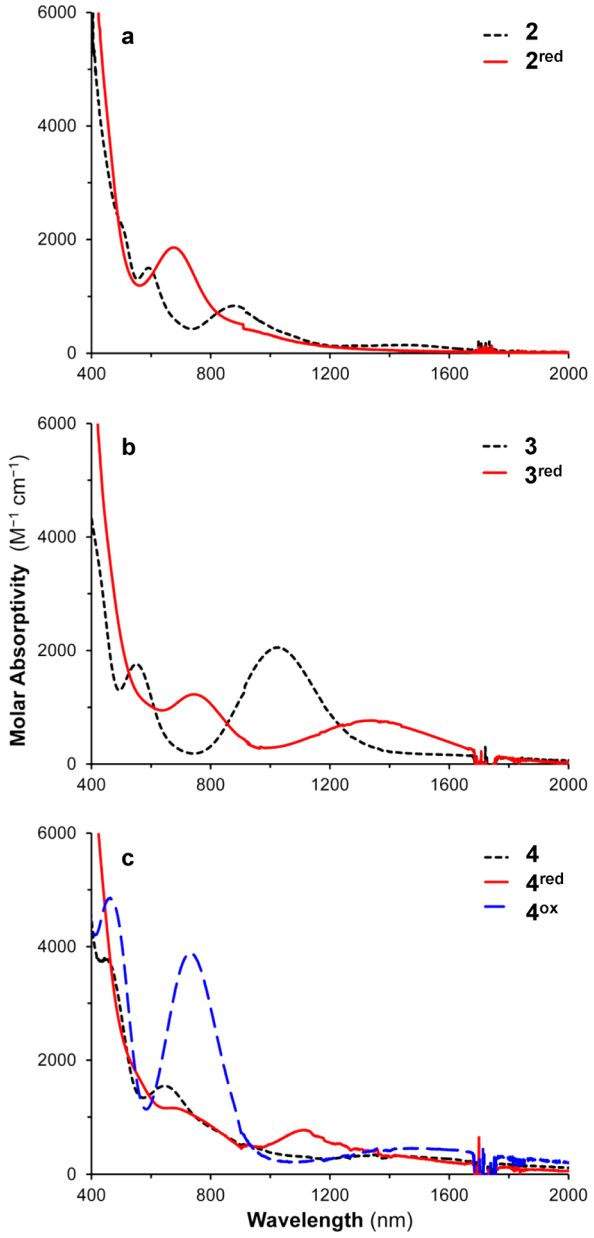

Figure 9. Vis–NIR plots for (a) **2** and $\mathbf{2}^{red}$; (b) **3** and $\mathbf{3}^{red}$; and (c) $\mathbf{4}^{ox}$, **4**, and $\mathbf{4}^{red}$ in THF at room temperature. Artifacts from solvent subtraction or light-source changes appear at ∼1750 nm.

The lowest-energy band observed for $\mathbf{2}^{red}$ has a λ_{max} value of 675 nm, or 14815 cm^{-1}. This band is assigned as the $\delta^4 \rightarrow \delta^3\delta^*$ excitation, and a resonance Raman (rR) study of $\mathbf{2}^{red}$ corroborates the assignment (vide infra). For **3**, the lowest-energy band is significantly shifted to lower energy by ∼5000 cm^{-1} to 1025 nm (9756 cm^{-1}). The dramatic decrease in the $\delta^4 \rightarrow \delta^3\delta^*$ transition energy upon formal substitution of Cr(I) with Mn(I) is unprecedented and might be a consequence of a smaller δ/δ^* splitting and/or larger exchange stabilization of the excited state in the case of heterobimetallic **3** versus homobimetallic $\mathbf{2}^{red}$.

To comprehend the electronic absorption spectra of the $(d-d)^{10}$ species, state-averaged CASSCF/PT2 and CASSI calculations were performed on the main configuration of $\mathbf{2}^{red\prime}$, **3′**, and $\mathbf{4}^{ox\prime}$ (Tables S15–S17, SI). Because these calculations are expensive, only the first six excitations were computed.

Table 8. Visible–NIR Electronic Absorbance Data for 2, $\mathbf{2}^{red}$, 3, $\mathbf{3}^{red}$, 4, $\mathbf{4}^{red}$, and $\mathbf{4}^{ox}$

complex	λ_{max} (nm)	ε (M^{-1} cm^{-1})
2	495	2330
	600	1480
	880	930
	1460	140
$\mathbf{2}^{red}$	675 (14815)[a]	1880
3	400	4400
	550	1850
	1025 (9756)[a]	2160
$\mathbf{3}^{red}$	745	1230
	1350	760
4	448	3640
	645	1440
	1344	220
$\mathbf{4}^{red}$	680	1200
	1110	7400
$\mathbf{4}^{ox}$	463	4860
	730	3890
	1495	490

[a]In wavenumbers (cm^{-1}).

Gratifyingly, $\delta^4 \rightarrow \delta^3\delta^*$ transitions were predicted for both $\mathbf{2}^{red\prime}$ and **3′**, and the transition energy for **3′** (673 nm) was correctly calculated to be lower than that for $\mathbf{2}^{red\prime}$ (545 nm). Although the absolute energies do not correspond well with the experimental values, the computed energy difference of 3500 cm^{-1} is in good agreement. For $\mathbf{4}^{ox\prime}$, $\delta \rightarrow \delta^*$-type transitions were notably absent, and the two low-lying transitions at 1006 and 1021 nm, which might correspond to the experimental band at 1495 nm, were $d_{Fe}^4 \rightarrow d_{Fe}^3\pi^*$ transitions. These findings validate the quintuple bonding in $\mathbf{2}^{red}$ and **3**, as well as the lower bond order in $\mathbf{4}^{ox}$.

Ground-state metal–metal vibrational frequencies are known for a handful of dichromium species,[56a,58] but to our knowledge, such data are lacking for any quintuply bonded complexes. To obtain MCr vibrational frequencies of quintuply bonded species, $\mathbf{2}^{red}$ and **3** were probed by resonance Raman (rR) spectroscopy. Excitation into the $\delta^4 \rightarrow \delta^3\delta^*$ band should selectively enhance the ν_{MCr} vibration. Indeed, irradiating a frozen sample of $\mathbf{2}^{red}$ at 647.1 nm afforded a series of low-frequency bands between 350 and 550 cm^{-1} (Figure 10), specifically at 363, 413, 434, and 495 cm^{-1}. The resonance enhancement of these modes was confirmed by the resultant depletion in their intensity when using a different wavelength (λ_{ex} = 514.5 nm) that is off-resonance with the $\delta^4 \rightarrow \delta^3\delta^*$ transition (Figure S18, SI).

The observation of multiple vibrations by rR spectroscopy can result from coupling of the ν_{MM} vibration with various ligand normal modes.[58b,59] Thus, we turned to DFT to elucidate the origin of the observed peaks. The DFT-calculated Raman spectrum of $\mathbf{2}^{red\prime}$ revealed four intense vibrations in the low-frequency region, whose spectral pattern and relative intensities are in good agreement with experiment. The calculated frequencies were 8–20% higher than the experimental ones, which is reasonable at the DFT level of theory.[60] To increase the accuracy of computed vibrational frequencies, a scale factor is commonly employed (see Computational Methods).[23] Hence, a scale factor of 0.88 was applied, giving the predicted Raman spectrum shown in Figure 10. The two most intense DFT-calculated vibrations at 416 and 443 cm^{-1}

DOI: 10.1021/acs.inorgchem.5b01163
Inorg. Chem. 2015, 54, 7579–7592

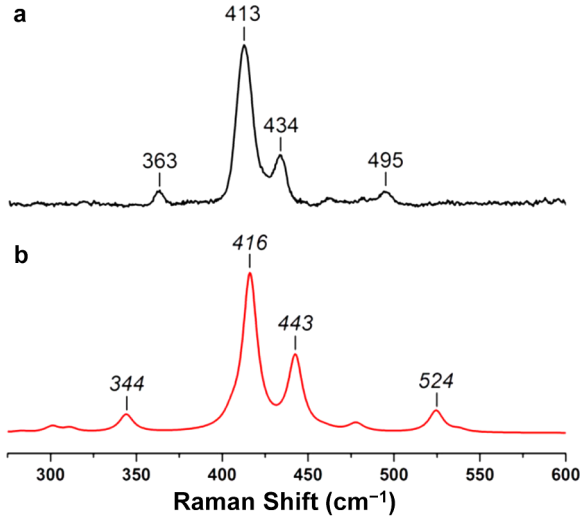

Figure 10. Stack plot of (a) the resonance Raman spectrum of $\mathbf{2}^{red}$ (10.4 mM in THF, λ_{ex} = 647.1 nm, 77 K) (black) and (b) the DFT-calculated Raman spectrum of $\mathbf{2}^{red\prime}$ (red).

are the asymmetric Cr—Cr—N_{ap} stretch and a relatively pure Cr—Cr vibration, respectively (Figures S20 and S21, SI). Thus, we assign the dichromium stretching frequency ν_{CrCr} at 434 cm^{-1} (corresponding to the calculated ν_{CrCr} value of 443 cm^{-1}). Of note, ν_{CrCr} values for quadruply bonded dichromium complexes are greater at 556 and 570 cm^{-1},[58a,c] despite having longer Cr—Cr bond distances (1.89, 2.11 Å vs 1.74 Å in $\mathbf{2}^{red}$). On the other hand, the naked dichromium molecule, which has a formal sextuple bond, also exhibits a relatively low ν_{CrCr} value of 481 cm^{-1}.[53] The lack of correspondence between bond order and ν_{CrCr} value might be due in part to the distorted potential energy surface of Cr_2, which has a minimum at 1.68 Å as well as a flat, shelf-like region at 2.5 Å.[39,61]

Finally, in contrast to $\mathbf{2}^{red}$, the isoelectronic manganese–chromium species **3** did not exhibit any enhanced nonsolvent features, precluding any determination of ν_{MnCr} (Figure S22, SI). However, the absence of ν_{MnCr} band(s) is reasonable considering that the $\delta^4 \rightarrow \delta^3\delta^*$ transition in **3** occurs at a longer wavelength that is currently beyond the range of our visible laser setup.

CONCLUSIONS

To better understand the nature of δ bonding, complexes with interactions between chromium and another mid-first-row transition metal (Cr, Mn, and Fe) were investigated. Specifically, bimetallics with $(d-d)^9$ to $(d-d)^{11}$ configurations were targeted to maximize the multiplicity of their metal–metal bond. The quintuply bonded complexes, $[Cr_2L]^-$ ($\mathbf{2}^{red}$) and MnCrL (**3**), have ultrashort M—Cr bonds, at 1.74 (r = 0.74) and 1.82 Å (r = 0.78), respectively. Complexes **2**, **4**, $\mathbf{4}^{ox}$, and $\mathbf{4}^{red}$ have r values of 0.82–0.84, which are in the range of triple to quadruple bonds. A $(d-d)^{10}$ configuration does not necessitate the formation of delta bond(s), as the FeCr complex $\mathbf{4}^{ox}$ lacks any. Also, deviations from the $(d-d)^{10}$ count can destroy δ bonds completely. The prototype MO picture of fivefold bonding would predict a formal bond order of 4.5 for $(d-d)^9$, but the experimental r value is more consistent with a lower bond order that is closer to 3. Finally, in contrast to the sensitive nature of δ bonds, σ and π bonds are quite robust in this series.

The spectroscopic characterization of this series also yielded some interesting findings. For instance, the diamagnetic anisotropy of metal–metal multiple bonds appears to be primarily affected by the polarity of the M—Cr bond, rather than its multiplicity. The $\delta^4 \rightarrow \delta^3\delta^*$ transition energy was red-shifted by over 5000 cm^{-1} by a simple metal-atom substitution, from $[Cr_2L]^-$ to MnCrL. The ν_{CrCr} value for quintuply bonded $[Cr_2L]^-$ was unexpectedly lower than those of the quadruply bonded analogues from the literature. In the $[FeCrL]^{+,0,-}$ redox series, the Mössbauer isomer shifts are consistent with the process

$$[Fe(I)Cr(III)L]^+ \xrightarrow{+e^-} Fe(0)Cr(III)L \xrightarrow{+e^-} [Fe(0)Cr(II)L]^-$$

The redox change from $[Fe(I)CrL]^+$ to Fe(0)CrL, however, manifests in significant bond changes not in the first coordination sphere of iron, but rather in that of chromium. Thus, assigning oxidation states based on changes in metal–ligand bond lengths, as revealed by X-ray crystallography, might be misleading in bimetallic systems with covalent metal–metal bonds and/or mixed amide–phosphine ligands.

ASSOCIATED CONTENT

Supporting Information

Additional spectroscopic and electrochemical characterization, as well as computational details. The Supporting Information is available free of charge on the ACS Publications website at DOI: 10.1021/acs.inorgchem.5b01163. Crystal structures have been deposited at the Cambridge Crystallographic Data Centre (CCDC) (1051668–1051672). They can be obtained free of charge from the CCDC at www.ccdc.cam.ac.uk/data_request/cif.

AUTHOR INFORMATION

Corresponding Authors

*E-mail: ebill@gwdg.de (E.B.).
*E-mail: gagliard@umn.edu (L.G.).
*E-mail: clu@umn.edu (C.C.L.).

Author Contributions

‡R.J.E. and P.A.R. contributed equally.

Notes

The authors declare no competing financial interest.

ACKNOWLEDGMENTS

The authors thank Carson Ingle for preliminary theoretical work, Bernd Mienert (Max Planck) for Mössbauer spectroscopic data collection, Ryan Cammarota for EPR collection, and Dr. Letitia Yao for NMR discussions. This experimental work was supported in part by the National Science Foundation (CHE-1254621) and the NIH (R13GM47365). C.C.L. thanks the Sloan Foundation. P.A.R. was supported by University of Minnesota (Doctoral Dissertation Fellowship) and the NSF-MRSEC program (DMR-0819885). X-ray diffraction experiments were performed using a crystal diffractometer acquired through an NSF–MRI award (CHE-1229400) in the X-ray laboratory supervised by Dr. Victor G. Young, Jr. The computational research (N.P., L.G., R.K.C.) was supported as part of the Inorganometallic Catalyst Design Center, an EFRC funded by the DOE, Office of Basic Energy Sciences (DE-SC0012702). R.K.C. was supported by a NSF graduate fellowship.

DOI: 10.1021/acs.inorgchem.5b01163
Inorg. Chem. 2015, 54, 7579–7592

REFERENCES

(1) Pauling, L. *The Nature of the Chemical Bond*, 3rd ed.; Cornell University Press: Ithaca, NY, 1960.

(2) (a) Mulliken, R. S. *Chem. Rev.* **1930**, *6*, 503−545. (b) Mulliken, R. S. *Chem. Rev.* **1931**, *9*, 347−388.

(3) (a) Cotton, F. A.; Curtis, N. F.; Harris, C. B.; Johnson, B. F. G.; Lippard, S. J.; Mague, J. T.; Robinson, W. R.; Wood, J. S. *Science* **1964**, *145*, 1305−1307. (b) Cotton, F. A.; Curtis, N. F.; Johnson, B. F. G.; Robinson, W. R. *Inorg. Chem.* **1965**, *4*, 326−330.

(4) (a) Morse, M. D. *Chem. Rev.* **1986**, *86*, 1049−1109. (b) Bondybey, V. E.; Schwartz, G. P.; English, J. H. *J. Chem. Phys.* **1983**, *78*, 11−15. (c) Spain, E. M.; Morse, M. D. *J. Phys. Chem.* **1992**, *96*, 2479−2486.

(5) (a) Brynda, M.; Gagliardi, L.; Roos, B. O. *Chem. Phys. Lett.* **2009**, *471*, 1−10. (b) Roos, B. O.; Borin, A. C.; Gagliardi, L. *Angew. Chem., Int. Ed.* **2007**, *46*, 1469−1472. (c) Malmqvist, P. Å.; Pierloot, K.; Shahi, A. R. M.; Cramer, C. J.; Gagliardi, L. *J. Chem. Phys.* **2008**, *128*, 204109/1−204109/10.

(6) (a) Nguyen, T.; Sutton, A. D.; Brynda, M.; Fettinger, J. C.; Long, G. J.; Power, P. P. *Science* **2005**, *310*, 844−847. (b) Radius, U.; Breher, F. *Angew. Chem., Int. Ed.* **2006**, *45*, 3006−3010.

(7) Nair, A. K.; Harisomayajula, N. V. S.; Tsai, Y.-C. *Dalton Trans.* **2014**, *43*, 5618−5638.

(8) (a) Wagner, F. R.; Noor, A.; Kempe, R. *Nat. Chem.* **2009**, *1*, 529−536. (b) Shen, J.; Yap, G. P. A.; Theopold, K. H. *J. Am. Chem. Soc.* **2014**, *136*, 3382−3384. (c) Tamne, E. S.; Noor, A.; Qayyum, S.; Bauer, T.; Kempe, R. *Inorg. Chem.* **2012**, *52*, 329−336. (d) Chen, H.-Z.; Liu, S.-C.; Yen, C.-H.; Yu, J.-S. K.; Shieh, Y.-J.; Kuo, T.-S.; Tsai, Y.-C. *Angew. Chem., Int. Ed.* **2012**, *51*, 10342−10346. (e) Schwarzmaier, C.; Noor, A.; Glatz, G.; Zabel, M.; Timoshkin, A. Y.; Cossairt, B. M.; Cummins, C. C.; Kempe, R.; Scheer, M. *Angew. Chem., Int. Ed.* **2011**, *50*, 7283−7286. (f) Chen, H.-G.; Hsueh, H.-W.; Kuo, T.-S.; Tsai, Y.-C. *Angew. Chem., Int. Ed.* **2013**, *52*, 10256−10260. (g) Noor, A.; Glatz, G.; Müller, R.; Kaupp, M.; Demeshko, S.; Kempe, R. *Nat. Chem.* **2009**, *1*, 322−325.

(9) (a) Krogman, J. P.; Thomas, C. M. *Chem. Commun.* **2014**, *50*, 5115−5127. (b) Kuppuswamy, S.; Bezpalko, M. W.; Powers, T. M.; Wilding, M. J. T.; Brozek, C. K.; Foxman, B. M.; Thomas, C. M. *Chem. Sci.* **2014**, *5*, 1617−1626. (c) Kuppuswamy, S.; Powers, T. M.; Krogman, J. P.; Bezpalko, M. W.; Foxman, B. M.; Thomas, C. M. *Chem. Sci.* **2013**, *4*, 3557−3565.

(10) (a) Clouston, L. J.; Siedschlag, R. B.; Rudd, P. A.; Planas, N.; Hu, S.; Miller, A. D.; Gagliardi, L.; Lu, C. C. *J. Am. Chem. Soc.* **2013**, *135*, 13142−13148. (b) Rudd, P. A.; Liu, S.; Planas, N.; Bill, E.; Gagliardi, L.; Lu, C. C. *Angew. Chem., Int. Ed.* **2013**, *52*, 4449−4452.

(11) Rudd, P. A.; Liu, S.; Gagliardi, L.; Young, V. G.; Lu, C. C. *J. Am. Chem. Soc.* **2011**, *133*, 20724−20727.

(12) Hughes, R. P.; Lindner, D. C.; Rheingold, A. L.; Yap, G. P. A. *Inorg. Chem.* **1997**, *36*, 1726−1727.

(13) Calderazzo, F.; Pampaloni, G.; Rocchi, L.; Englert, U. *Organometallics* **1994**, *13*, 2592−2601.

(14) Brookhart, M.; Grant, B.; Volpe, A. F., Jr. *Organometallics* **1992**, *11*, 3920−3922.

(15) McConnell, H. M.; Holm, C. H. *J. Chem. Phys.* **1957**, *27*, 314−315.

(16) Pregosin, P. S. *NMR in Organometallic Chemistry*; Wiley-VCH: Weinheim, Germany, 2012.

(17) Sheldrick, G. M. *SADABS*; University of Göttingen: Göttingen, Germany, 1997.

(18) (a) Sheldrick, G. M.; Schneider, T. R. *Macromol. Crystallogr. B* **1997**, *277*, 319. (b) Sheldrick, G. M. *Acta Crystallogr. A* **2008**, *64*, 112−122.

(19) Spek, A. L. *Acta Crystallogr. D* **2009**, *65*, 148−155.

(20) (a) Perdew, J. P.; Burke, K.; Ernzerhof, M. *Phys. Rev. Lett.* **1996**, *77*, 3865−3868. (b) Ahlrichs, R.; Bar, M.; Haser, M.; Horn, H.; Kolmel, C. *Chem. Phys. Lett.* **1989**, *162*, 165−169. (c) *TURBOMOLE 6.4*; TURBOMOLE GmbH: Karlsruhe, Germany, 2012; available at http://www.turbomole.com.

(21) Schäfer, A.; Huber, C.; Ahlrichs, R. *J. Chem. Phys.* **1994**, *100*, 5829−5835.

(22) Eichkorn, K.; Treutler, O.; Öhm, H.; Häser, M.; Ahlrichs, R. *Chem. Phys. Lett.* **1995**, *240*, 283−290.

(23) (a) Alecu, I. M.; Zheng, J.; Zhao, Y.; Truhlar, D. G. *J. Chem. Theory Comput.* **2010**, *6*, 2872−2887. (b) Laury, M. L.; Carlson, M. J.; Wilson, A. K. *J. Comput. Chem.* **2012**, *33*, 2380−2387.

(24) (a) Roos, B. O.; Taylor, P. R.; Siegbahn, P. E. M. *Chem. Phys.* **1980**, *48*, 157−173. (b) Andersson, K.; Malmqvist, P. Å.; Roos, B. O. *J. Chem. Phys.* **1992**, *96*, 1218−1226. (c) Andersson, K.; Malmqvist, P. Å.; Roos, B. O.; Sadlej, A. J.; Wolinski, K. *J. Phys. Chem.* **1990**, *94*, 5483−5488. (d) Aquilante, F.; De Vico, L.; Ferré, N.; Ghigo, G.; Malmqvist, P.-Å.; Neogrady, P.; Pedersen, T.; Pitonak, M.; Reiher, M.; Roos, B. O.; Serrano-Andrés, L.; Urban, M.; Veryazov, V.; Lindh, R. *J. Comput. Chem.* **2010**, *31*, 224−247.

(25) Douglas, M.; Kroll, N. M. *Ann. Phys.* **1974**, *82*, 89−155.

(26) (a) Roos, B. O.; Lindh, R.; Malmqvist, P. Å.; Veryazov, V.; Widmark, P. O. *J. Phys. Chem. A* **2004**, *108*, 2851−2858. (b) Roos, B. O.; Lindh, R.; Malmqvist, P. Å.; Veryazov, V.; Widmark, P. O. *J. Phys. Chem. A* **2005**, *109*, 6575−6579.

(27) (a) Aquilante, F.; Malmqvist, P.-A.; Pedersen, T. B.; Ghosh, A.; Roos, B. O. *J. Chem. Theory Comput.* **2008**, *4*, 694−702. (b) Aquilante, F.; Pedersen, T. B.; Lindh, R. *J. Chem. Phys.* **2007**, *126*, 194106/1−194106−10. (c) Aquilante, F.; Pedersen, T. B.; Lindh, R.; Roos, B. O.; de Meras, A. S.; Koch, H. *J. Chem. Phys.* **2008**, *129*, 24113−24118.

(28) Gagliardi, L.; Lindh, R.; Karlström, G. *J. Chem. Phys.* **2004**, *121*, 4494−4500.

(29) (a) Malmqvist, P. Å. *Int. J. Quantum Chem.* **1986**, *30*, 479. (b) Malmqvist, P.-Å.; Roos, B. O. *Chem. Phys. Lett.* **1989**, *155*, 189−194.

(30) The order of addition is important for the selective synthesis of MnCrL (**3**). If $MnBr_2$ is stirred with CrL first, the Cr_2L byproduct forms. Adding KC_8 prior to $MnBr_2$ effectively prevents the formation of any detectable amount of Cr_2L.

(31) Sircoglou, M.; Bontemps, S.; Bouhadir, G.; Saffon, N.; Miqueu, K.; Gu, W.; Mercy, M.; Chen, C.-H.; Foxman, B. M.; Maron, L.; Ozerov, O. V.; Bourissou, D. *J. Am. Chem. Soc.* **2008**, *130*, 16729−16738.

(32) (a) Casey, A. T.; Mitra, S. Magnetic Behavior of Components Containing d^n Ions. In *Theory and Applications of Molecular Paramagnetism*, Boudreaux, E. A., Mulay, L. N., Eds.; John Wiley & Sons: New York, 1976; pp 135−255. (b) Dalal, N. S.; Murillo, C. A. *Dalton Trans.* **2014**, *43*, 8565−8576.

(33) Cummings, D. A.; McMaster, J.; Rieger, A. L.; Rieger, P. H. *Organometallics* **1997**, *16*, 4362−4368.

(34) Evans, D. F. *J. Chem. Soc.* **1959**, 2003−2005.

(35) (a) Wolf, R.; Ni, C.; Nguyen, T.; Brynda, M.; Long, G. J.; Sutton, A. D.; Fischer, R. C.; Fettinger, J. C.; Hellman, M.; Pu, L.; Power, P. P. *Inorg. Chem.* **2007**, *46*, 11277−11290. (b) Noor, A.; Wagner, F. R.; Kempe, R. *Angew. Chem., Int. Ed.* **2008**, *47*, 7246−7249. (c) Noor, A.; Glatz, G.; Müller, R.; Kaupp, M.; Demeshko, S.; Kempe, R. *Z. Anorg. Allg. Chem.* **2009**, *635*, 1149−1152. (d) Noor, A.; Bauer, T.; Todorova, T. K.; Weber, B.; Gagliardi, L.; Kempe, R. *Chem.—Eur. J.* **2013**, *19*, 9825−9832. (e) Kreisel, K. A.; Yap, G. P. A.; Dmitrenko, O.; Landis, C. R.; Theopold, K. H. *J. Am. Chem. Soc.* **2007**, *129*, 14162−14163. (f) Hsu, C.-W.; Yu, J.-S. K.; Yen, C.-H.; Lee, G.-H.; Wang, Y.; Tsai, Y.-C. *Angew. Chem., Int. Ed.* **2008**, *47*, 9933−9936. (g) Wu, L.-C.; Hsu, C.-W.; Chuang, Y.-C.; Lee, G.-H.; Tsai, Y.-C.; Wang, Y. *J. Phys. Chem. A* **2011**, *115*, 12602−12615. (h) Huang, Y.-L.; Lu, D.-Y.; Yu, H.-C.; Yu, J.-S. K.; Hsu, C.-W.; Kuo, T.-S.; Lee, G.-H.; Wang, Y.; Tsai, Y.-C. *Angew. Chem., Int. Ed.* **2012**, *51*, 7781−7785.

(36) (a) Pauling, L. *J. Am. Chem. Soc.* **1947**, *69*, 542−553. (b) Cordero, B.; Gomez, V.; Platero-Prats, A. E.; Reves, M.; Echeverria, J.; Cremades, E.; Barragan, F.; Alvarez, S. *Dalton Trans.* **2008**, 2832−2838.

(37) Chasteen, N. D.; Belford, R. L. *Inorg. Chem.* **1970**, *9*, 169−175.

(38) Tsai, Y.-C.; Hsu, C.-W.; Yu, J.-S. K.; Lee, G.-H.; Wang, Y.; Kuo, T.-S. *Angew. Chem., Int. Ed.* **2008**, *47*, 7250−7253.

(39) Casey, S. M.; Leopold, D. G. *J. Phys. Chem.* **1993**, *97*, 816−830.

DOI: 10.1021/acs.inorgchem.5b01163
Inorg. Chem. 2015, 54, 7579−7592

(40) (a) Bondybey, V. E.; English, J. H. *Chem. Phys. Lett.* **1983**, *94*, 443−447. (b) Michalopoulos, D. L.; Geusic, M. E.; Hansen, S. G.; Powers, D. E.; Smalley, R. E. *J. Phys. Chem.* **1982**, *86*, 3914−3916. (c) Efremov, Y. M.; S, A. N.; Gurvich, L. V. *Opt. Spectrosc.* **1974**, *36*, 381−382.
(41) Cotton, F. A. Chromium Compounds. In *Multiple Bonds between Metal Atoms*; Cotton, F. A., Murillo, C. A., Walton, R. A., Eds.; Springer Science: New York, 2005; pp 35−68.
(42) Cotton, F. A. Physical, Spectroscopic, and Theoretical Results. In *Multiple Bonds between Metal Atoms*; Cotton, F. A., Murillo, C. A., Walton, R. A., Eds.; Springer Science: New York, 2005; pp 707−796.
(43) (a) Cotton, F. A.; Daniels, L. M.; Murillo, C. A.; Pascual, I.; Zhou, H.-C. *J. Am. Chem. Soc.* **1999**, *121*, 6856−6861. (b) Mashima, K.; Tanaka, M.; Tani, K.; Nakamura, A.; Takeda, S.; Mori, W.; Yamaguchi, K. *J. Am. Chem. Soc.* **1997**, *119*, 4307−4308.
(44) (a) McGlinchey, M. J. *Inorg. Chem.* **1980**, *19*, 1392−1394. (b) San Filippo, J. *Inorg. Chem.* **1972**, *11*, 3140−3143. (c) Agaskar, P. A.; Albert Cotton, F. *Polyhedron* **1986**, *5*, 899. (d) Cotton, F. A.; Kitagawa, S. *Polyhedron* **1988**, *7*, 1673−1676.
(45) The methyl groups also display substantial magnetic anisotropy and split into four unique resonances at −40 °C. The methyl resonances in NiAlL span a 0.26 ppm range (from 1.08 to 0.84 ppm), whereas the methyl groups span 1.58 ppm in $\mathbf{2}^{red}$ (from 1.85 to 0.27 ppm), 1.31 ppm in **3**, and 1.06 ppm in $\mathbf{4}^{ox}$. A wider range indicates that the isopropyl groups are located within the shielded and deshielded zones.
(46) Balazs, G.; Cloke, F. G. N.; Gagliardi, L.; Green, J. C.; Harrison, A.; Hitchcock, P. B.; Shahi, A. R. M.; Summerscales, O. T. *Organometallics* **2008**, *27*, 2013−2020.
(47) (a) Cotton, F. A.; James, C. A. *Inorg. Chem.* **1992**, *31*, 5298−5307. (b) Cotton, F. A.; Ren, T. *J. Am. Chem. Soc.* **1992**, *114*, 2237−2242. (c) Cotton, F. A.; Eglin, J. L.; James, C. A. *Inorg. Chem.* **1993**, *32*, 681−686.
(48) Cotton, F. A.; Dunbar, K. R.; Hong, B.; James, C. A.; Matonic, J. H.; Thomas, J. L. C. *Inorg. Chem.* **1993**, *32*, 5183−5187.
(49) Harris, R. K. *Nuclear Magnetic Resonance Spectroscopy: A Physiocochemical View*; Longman: London, 1986.
(50) (a) Brynda, M.; Gagliardi, L.; Widmark, P.-O.; Power, P. P.; Roos, B. O. *Angew. Chem., Int. Ed.* **2006**, *45*, 3804−3807. (b) La Macchia, G.; Aquilante, F.; Veryazov, V.; Roos, B. O.; Gagliardi, L. *Inorg. Chem.* **2008**, *47*, 11455−11457. (c) La Macchia, G.; Li Manni, G.; Todorova, T. K.; Brynda, M.; Aquilante, F.; Roos, B. O.; Gagliardi, L. *Inorg. Chem.* **2010**, *49*, 5216−5222.
(51) (a) Neese, F. *Inorg. Chim. Acta* **2002**, *337*, 181−182. (b) Neese, F.; Petrenko, T. Quantum Chemistry and Mössbauer Spectroscopy. In *Mössbauer Spectroscopy and Transition Metal Chemistry: Fundamentals and Applications*; Gütlich, P.; Bill, E.; Trautwein, A. X., Eds.; Springer: Berlin, 2011; pp 137−199.
(52) Berry, J. F.; Bill, E.; Bothe, E.; George, S. D.; Mienert, B.; Neese, F.; Wieghardt, K. *Science* **2006**, *312*, 1937−1941.
(53) (a) Rittle, J.; Peters, J. C. *Proc. Natl. Acad. Sci. U.S.A.* **2013**, *110*, 15898. (b) Lee, Y.; Mankad, N. P.; Peters, J. C. *Nat. Chem.* **2010**, *2*, 558−565. (c) Lee, Y.; Peters, J. C. *J. Am. Chem. Soc.* **2011**, *133*, 4438−4446.
(54) Rudd, P. A.; Planas, N.; Bill, E.; Gagliardi, L.; Lu, C. C. *Eur. J. Inorg. Chem.* **2013**, *2013*, 3898−3906.
(55) Gütlich, P., Bill, E., Trautwein, A. X., Eds. *Mössbauer Spectroscopy and Transition Metal Chemistry: Fundamentals and Applications*; Springer: Berlin, 2011.
(56) (a) Manning, M. C.; Trogler, W. C. *J. Am. Chem. Soc.* **1983**, *105*, 5311. (b) Belforte, A.; Belli Dell'Amico, D.; Calderazzo, F.; Devillers, M.; Englert, U. *Inorg. Chem.* **1993**, *32*, 2282−2286.
(57) Zall, C. M.; Zherebetskyy, D.; Dzubak, A. L.; Bill, E.; Gagliardi, L.; Lu, C. C. *Inorg. Chem.* **2012**, *51*, 728−736.
(58) (a) Hsiao, C.-J.; Lai, S.-H.; Chen, I. C.; Wang, W.-Z.; Peng, S.-M. *J. Phys. Chem. A* **2008**, *112*, 13528−13534. (b) Da Re, R. E.; Eglin, J. L.; Carlson, C. N.; John, K. D.; Morris, D. E.; Woodruff, W. H.; Bailey, J. A.; Batista, E.; Martin, R. L.; Cotton, F. A.; Hillard, E. A.; Murillo, C. A.; Sattelberger, A. P.; Donohoe, R. J. *J. Am. Chem. Soc.* **2010**, *132*, 1839−1847. (c) Cotton, F. A.; Fanwick, P. E.; Niswander, R. H.; Sekutowski, J. C. *J. Am. Chem. Soc.* **1978**, *100*, 4725−4732.
(59) (a) John, K. D.; Miskowski, V. M.; Vance, M. A.; Dallinger, R. F.; Wang, L. C.; Geib, S. J.; Hopkins, M. D. *Inorg. Chem.* **1998**, *37*, 6858−6873. (b) Clark, R. J. H.; Firth, S.; Sella, A.; Miskowski, V. M.; Hopkins, M. D. *J. Chem. Soc., Dalton Trans.* **2000**, 2928−2932. (c) Chisholm, M. H.; Cotton, F. A.; Frenz, B. A.; Reichert, W. W.; Shive, L. W.; Stults, B. R. *J. Am. Chem. Soc.* **1976**, *98*, 4469−4476. (d) Chisholm, M. H.; Cotton, F. A.; Extine, M.; Stults, B. R. *J. Am. Chem. Soc.* **1976**, *98*, 4477−4485.
(60) Cramer, C. J.; Truhlar, D. G. *Phys. Chem. Chem. Phys.* **2009**, *11*, 10757−10816.
(61) (a) Dachsel, H.; Harrison, R. J.; Dixon, D. A. *J. Phys. Chem. A* **1998**, *103*, 152. (b) Moskovits, M.; Limm, W.; Mejean, T. *J. Phys. Chem.* **1985**, *89*, 3886−3890.

DOI: 10.1021/acs.inorgchem.5b01163
Inorg. Chem. 2015, 54, 7579−7592